Army Research Laboratory

Turbulence Simulation: On Phase and Deflector Screen Generation

By
David H. Tofsted

Computational & Information Sciences Directorate
Battlefield Environment Division

ARL-TR-1886 October 2001

NOTICES

Disclaimers

The findings in this report are not to be construed as an official Department of the Army position, unless so designated by other authorized documents.

Citation of manufacturers' or trade names does not constitute an official endorsement or approval of the use thereof.

REPORT DOCUMENTATION PAGE

Form Approved
OMB No. 0704-0188

1. AGENCY USE ONLY (*Leave Blank*)	2. REPORT DATE	3. REPORT TYPE AND DATES COVERED
	October 2001	Technical Report, October 2001

4. TITLE AND SUBTITLE

Turbulence Simulation: On Phase and Deflector Screen Generation

5. FUNDING NUMBERS

6. AUTHOR(S)

David H. Tofsted

7. PERFORMING ORGANIZATION NAME(S) AND ADDRESS(ES)

U.S. Army Research Laboratory
Computational & Information Sciences Directorate
Battlefield Environment Division
ATTN: AMSRL-CI-EW
White Sands Missile Range, NM 88002-5501

8. PERFORMING ORGANIZATION REPORT NUMBER

ARL-TR-1886

9. SPONSORING/MONITORING AGENCY NAME(S) AND ADDRESS(ES)

U.S. Army Research Laboratory
2800 Powder Mill Road
Adelphi, MD 20783-1145

10. SPONSORING/MONITORING AGENCY REPORT NUMBER

ARL-TR-1886

11. SUPPLEMENTARY NOTES

12a. DISTRIBUTION/AVAILABILITY STATEMENT

Approved for public release; distribution unlimited.

12b. DISTRIBUTION CODE

A

13. ABSTRACT (Maximum 200 words)

This report examines the topic of phase screen generation and introduces an alternative method of modeling propagation through turbulence based on an extended raytrace method involving passage through three-dimensionally varying refractive turbulence. The mathematics of propagation through turbulence are thoroughly detailed, including several derivations often left as exercises for the reader in other documentation. Chapter 2 contains an analysis of the interrelationships between Fourier transforms, Fourier series, and Fast Fourier Transform (FFT) methods. These methods are used in chapter 3 to describe means of transforming between common mathematical forms of turbulence spectra used in the literature and standard engineering forms for employing FFTs. Chapter 4 concludes with an analysis of phase screen and deflector screen generation and usage.

14. SUBJECT TERMS

propagation, turbulence, outer scale, image distortion

15. NUMBER OF PAGES

75

16. PRICE CODE

17. SECURITY CLASSIFICATION OF THIS REPORT	18. SECURITY CLASSIFICATION OF THIS PAGE	19. SECURITY CLASSIFICATION OF ABSTRACT	20. LIMITATION OF ABSTRACT
UNCLASSIFIED	UNCLASSIFIED	UNCLASSIFIED	SAR

Preface

The problem of modeling optical turbulence effects within target acquisition models has largely been limited to characterizing the influence of turbulent blur on the modulation transfer function (MTF) for the system under study. However, as useful as this characterization may be, the effects of turbulence are often not limited to the MTF alone. The MTF is only one of three turbulence effects on impacting sensing systems.

The remaining two effects are normally described as scintillation and angle-of-arrival variations. Scintillation causes temporal fluctuations in received intensity across a target and/or background. The most obvious example of scintillation can be seen when approaching an oncoming vehicle on the highway. A glint portion of the vehicle (usually a sun reflection from the vehicle windshield) appears to fluctuate in brightness. Scintillation is usually unimportant for objects of near-uniform brightness, but the appearance of hot spots (glint features) will be significantly influenced by scintillation effects. The influence of scintillation can be considered a contributor to the overall noise within an atmosphere-optics-electronics-human detection system.

Further, system designers tend to develop systems which suppress scintillation effects. The log variance of scintillation varies as $k^{7/6}$, where k is the radiation wavenumber $2\pi/\lambda$. Systems operating at longer wavelengths experienced significantly reduced scintillation effects compared to visible systems. Receiver aperture diameter also influences the scintillation. For large receiver optics the scintillation is aperture averaged. Hence, more scintillation is seen by the human eye than through a telescope at the same wavelength. There is, however, a tradeoff between scintillation and atmospheric blurring effects. Larger apertures that tend to reduce scintillation also tend to cause increased turbulent blurring.

At infrared (IR) wavelengths both scintillation and blurring effects are reduced, yet turbulence effects are still a factor due to image distortion. In the far IR, angle-of-arrival fluctuations are the more pervasive turbulence influence. Also known as image wander, shimmer, heat boil, and jitter, angle-of-arrival fluctuations are the first noticable turbulent distortion.

Currently, angle-of-arrival influences are not considered in target acquisition models. The reason for this deficiency is rather simple: Systems analysis models generally utilize linear shift invariant (LSI) assumptions. Angle of arrival effects are not LSI because of a related parameter called the isoplanatic patch size, θ_0. When θ_0 is large, scene objects appear to move in position due to angle-of-arrival fluctuations, yet tend to maintain their structural coherence because the

same error applies to every point in the object. But as θ_0 shrinks in angular extent below the angular subtense of an object of interest, different portions of the object appear to shift independently in angle relative to one another. The effects of such a distortion on an observer's ability to percieve the object then involves a complex interaction between object characteristics, background characteristics, and the qualities of the perturbations. It becomes necessary to conduct observer tests to determine the gestalt of the entire process on the ability of the observer to understand the fluctuating scene. In the end it may be possible to assign complexity values, similar to the N_{50} values used in target acquisition codes, to evaluate the degrading effects of the image distortion on the observer capabilities. These observer tests will require simulation of image distortion through an image modification code.

This paper provides support for calculations needed in such image distortion codes. In it, we describe a method of modifying images for angle-of-arrival distortion and for the more standard phase screen approach. To perform either of these tasks properly requires knowledge of the appropriate spatial frequency spectrum of the turbulent fluctuations, and knowledge of the means of representing these fluctuations in a model of the atmosphere. One must then define a method of image manipulation which supports the calculation of distorted images from undistorted source images. This text discusses use of a turbulence spectrum developed recently which handles both inner and outer scale influences on the refractive index spectrum within the earth's surface layer atmosphere.

Acknowledgements

The modeling of turbulence effects on image propagation is a difficult issue. The math is nontrivial. As such, a careful review was necessary. Approximations used were scrutinized, and where necessary, more precise language was suggested by my reviewers: Drs. David Marlin and Edward Measure. Their assistance in improving this document was invaluable.

I'd also like to thank Carlos Marrero, visiting student from Puerto Rico under the auspices of the Hispanic Alliance of Colleges and Universities. His assistance in coding the calculations needed to evaluate the beam width effects (shown in figures 5 and 6) helped close a final gap in the text. Lastly, I'd like to thank Dr. Sean O'Brien who provided a ready ear while I worked through the image distortion analysis and dealt with reviewer comments.

Table of Contents

Figures

Executive Summary

Rationale

Forward-Looking Infrared (FLIR) devices have been a part of the Army inventory for over twenty years. In that time the state-of-the-art in FLIR technology has improved significantly. We are now using third-generation FLIR devices, which exhibit significantly lower noise and higher spatial resolution than was possible twenty years ago. However, with that increased resolution has come the realization that turbulence effects are not minimal when compared with the system noise in these new sensors. Further, the next generation of FLIRs will likely involve higher magnification devices designed for specialty applications such as narrow fields of regard. To enable such applications, the sensor aperture diameter may need to be increased, leading to larger amounts of turbulent blur on the received imagery. Lower noise thresholds and higher resolution detection grids often means being able to detect image distortion due to angle-of-arrival fluctuations.

Because of these concerns, and because current sensor performance prediction models do not incorporate turbulence effects, it is reasonable to attempt to simulate turbulence effects in a modeling environment. Traditionally, analysis of turbulence effects has followed the course of incorporating turbulent blur effects as a multiplicative atmospheric turbulence Modulation Transfer Function (MTF) when combined with the system MTF. However, for FLIR systems the chief turbulence concern may be apparent object shape distortion and this effect, because it is not shift invariant, cannot be modeled via an MTF. Rather, it must be modeled using image processing techniques.

Analyses

To support these image processing techniques, one must develop a methodology akin to methods originally developed for high energy laser simulations. The principle method developed in the 1970's to study these propagation problems involved mathematical constructs known as phase screens. While the literature on phase screens is somewhat extensive, certain key elements of the analyses in this literature involve undeveloped assumptions, certain mathematical flaws,

and exercises left to the reader. This approach did not seem satisfactory, leading to the development of this document.

In this document we explore the basic equations necessary to describe Fourier transforms, Fourier series expansions, and the fundamental equations undergirding the Fast Fourier Transform technique. Because these methods are essentially related, we show the means of transforming results obtained by one Fourier method into its equivalent representation under another form. We thus permit conversions (without disturbing questions about suitability and applicability) between different forms of these Fourier methods used in different parts of the literature. In particular, the turbulence literature uses significantly different nomenclature and transform techniques from the propagation literature. Suitable transforms are possible when the turbulence results have been translated into propagation literature form. These processes constitute the bulk of chapters 2 and 3. In chapter 4 these techniques are applied to the problems of phase and deflector screen propagation.

Chapter 4 contains an overview of the phase screen generation and derivation process. Phase screens have been used in the past largely in beam-wave applications. Our interest in image modification requires working with large area effects. To support this goal, a less computationally intensive deflector screen method is introduced. This method extends prior refractive raytracing and mirage imaging techniques that handled only vertical inhomogeneities in the refractive index structure for fully three-dimensional effects.

Conclusions

In this report, the mathematics of several key concepts are developed in support of simulating turbulence effects on image propagation. As a result of these developments the underlying means of translating between different forms of the Fourier transform was shown. This development permitted the writing of the turbulence spectrum in terms that can be used in computer representation of turbulence effects. In combination with an analysis of both the phase screen methodology and the deflector screen approach, we showed that large scale turbulence can have significant effects on image distortion. A means was also discovered for handling finite sized incoherent source regions emitting energy that is received at a circular aperture. The resulting analysis showed that high frequency turbulence has little effect on image shape distortion. The result of these analyses is a method for distorting imagery for heat boil type turbulence distortion effects. These effects essentially consist of a combination of angle-of-arrival fluctuations which distort apparent object location and isoplanatism which causes different portions of the scene to distort in different directions.

1. Introduction

Recent developments in optics have resulted in sensors of increasing sensitivity at infrared (IR) wavelengths with significantly reduced noise that often limited earlier devices. This has caused an increased awareness within the IR sensor development community that turbulence effects should be included in sensor performance models.

In particular, turbulent image distortion can be significant for IR wavelength imagery. However, the modeling tools to simulate distortion effects have been nonexistent. One reason for this deficiency is that prior research in the turbulence area has focused on astronomical problems, involving plane wave propagation, narrow fields of view, large aperture sizes, and low turbulence. By comparison, the Army problem of point-to-point observation in which observers attempt to acquire and track targets near the ground usually involves spherical wave propagation, wide fields of view, aperture sizes close to the Fresnel zone in diameter, and high turbulence. For point-to-point observations with both object and observer located near the earth's surface, significant optical turbulence effects may be encountered. For astronomical problems, the observation site is usually selected to avoid as much turbulence as possible. Often the observatory is thermally controlled to avoid temperature differences between the outside atmosphere and the entrance pupil to the telescope. Such luxuries are not possible for Army operations.

Flat desert conditions, for example, can cause extreme turbulence conditions. When discussing turbulence viewing with Army and Marine officers at Ft. Knox, KY, some years ago, a comment was made that targets more distant than approximately 1 km were simply not engaged because the amount of turbulent distortion and blur present made it nearly impossible to identify targets at longer ranges. At IR wavelengths, turbulence effects are considerably less than at visible wavelengths and so there is the hope that IR sensors will ultimately provide better performance under high turbulence conditions. The question is how much better? And can certain tradeoffs or adaptive optics further improve sensor performance? The only way to quantitatively answer such questions is through accurate modeling of turbulence effects and human perception testing to determine how observers interpret distorted or partially corrected signals. Modeling synthetic scenes including both system and turbulence effects means the ability to perform perception testing under controlled conditions. Planned adaptive optics augmentation of sensors can also be tested. The addition of adaptive optics merely makes the sensors more complicated and extends the modeling required to simulate the image acquisition process. Such a system

would still have to be evaluated in terms of its ability to compensate for turbulence effects, and human testing would still be required to determine the efficacy and cost effectiveness of such methods.

One key concern in determining turbulence effects is to adequately model the differences in turbulence effects over a range of turbulence strengths. In this report we discuss methodologies for simulating turbulence within image-rendering software. While this topic is not new, prior efforts have been primarily related to image blur effects only. Here, the focus is on image distortion.

This effort has strong links to prior efforts to understand turbulence effects on beam wave propagation. Unfortunately that literature is not as well documented as might be imagined. While several studies have been conducted in the area of beam wave propagation, there are errors within the standard documentation. Later papers have simply repeated these errors, while others have provided correct equations without providing the basis for these results. A general presentation of turbulence propagation methods is thus in order, a presentation which attempts to generate seamless and consistent, error-free results, while discussing the various caveats and limitations involved. In addition, a method based on raytracing technology is discussed that should provide nearly the same fidelity of calculation as is available from the standard phase screen methods without the significant cost in computational time necessary to handle the propagation of incoherent light at the level of tracking the propagation of field amplitudes.

To accomplish this analysis task, we establish the nature of the Fourier transform and its relationship to other Fourier relations. This first step is designed to support a transformation of results between different, but related, standards used in the literature. This literature crosses several disciplinary boundaries, from micrometeorology to statistics to optics to computational methods. Each of these disciplines has individualized means of representing Fourier objects. The separate disciplines must be examined and interrelated to smoothly translate between the different forms. In particular, to represent the Fourier version of the refractive index power spectrum for optical turbulence, one must be able to (1) translate between two forms of the Fourier transform, and (2) express these results in a form compatible with the inverse Fourier transform using a Fast Fourier method. This process involves converting the Fourier transform of a continuous function to a Fourier series coefficient set compatible with the periodic functions and limited frequency regime of the Fast Fourier Transform. This form must be compatible with a propagation code that handles sensor optics and the diffraction propagation between turbulence phase screens. To support these various developments, the main analyses have been divided between chapters: Fourier methods in chapter 2, turbulence representation in chapter 3, and propagation methods in chapter 4.

2. Fourier Analysis

In this chapter we discuss Fourier representations of various types of functions. As will be seen, representing these functions in terms of sinusoidal components yields different results depending on the nature of the functions themselves. These differences are of interest because of the various ways that turbulence needs to be or has been represented in different settings.

In particular, in previous studies of optical turbulence structure (cf. Beland, 1993) the refractive index spectrum was viewed as space filling. However, we know that fluctuations in the refractive index near the earth's surface do not extend upward significantly. Further, the strength of turbulence is likely a horizontally varying quantity. Hence, although studies of turbulence simulation discuss the nature of the turbulence in terms of abstract, infinite fields of turbulence, when treating numerical turbulence within finite computers, the turbulence representation is always finite. Here we define the term "field" as a multi-dimensionally varying random function which obeys certain statistical properties. Often, in describing the temporal nature of turbulence fields, Taylor's hypothesis is used whereby the turbulence is considered "frozen" such that it advects with the mean wind but otherwise does not change its spatial fluctuational structure.

In terms of finite computers, the turbulence structure is specified, limits are applied, and fields are simulated using either hardware or gridded data sets which are limited in extent. Thus, Fourier series representations are used rather than Fourier transforms (Andrews and Shivamoggi, 1999), and these series are represented in such a way as to be computed by fast computational methods.

For many readers, much of this chapter will be a review, but the information is introduced to develop a common framework for discussion and to introduce terminology and the particular form used for the Fast Fourier Transform (FFT).

In using the FFT method, the modeled volume of the turbulent region is assumed to be periodic in three dimensions. The analysis, then, needs to consider a three-dimensional problem. However, our analysis will begin by studying a one-dimensional case and then extending the results to three dimensions. The x axis is chosen for the analysis, but the properties discussed will be the same on each of the other axes following changes in axis labels and integration limits.

2.1 Gaskill's Fourier Transform

We begin by discussing a form of the Fourier transform (Gaskill, 1978) that has symmetric forward and inverse transform equations. This form will be followed closely when considering the Fourier series representation for periodic functions. The results of these considerations will then be used in relating the transforms currently adopted in the turbulence literature to the forms needed to represent phase screens using an FFT approach.

2.1.1 Transform Definition

According to Gaskill (1978), the Fourier transform is defined as

$$F(\xi) = \int_{-\infty}^{\infty} f(x) \exp(-i\,2\pi\,x\,\xi)\; dx. \tag{1}$$

One can then recover the original function, $f(x)$, through the inverse transform

$$f(x) = \int_{-\infty}^{\infty} F(\xi) \exp(i\,2\pi\,x\,\xi)\; d\xi. \tag{2}$$

The function $F(\xi)$ is called the Fourier transform of the function $f(x)$, and similarly the function $f(x)$ is called the inverse transform of $F(\xi)$. Note the symmetry involved in Gaskill's version of the Fourier transform. Other forms, including those used in much of the turbulence literature, involve external 2π factors in either the transform or inverse transform process. (In fact, in some of the literature, the transformed functions are not called Fourier transforms at all. Instead, they are referred to as characteristic functions (Papoulis, 1984; Panofsky and Dutton, 1984).)

Under Gaskill's transform definition, a dilated and shifted function transforms as

$$f\left(\frac{x \pm x_0}{a}\right) \stackrel{\mathcal{F}}{\Longrightarrow} |a| \exp(\pm i\,2\pi\,x_0\,\xi)\; F(a\xi), \tag{3}$$

where $\stackrel{\mathcal{F}}{\Longrightarrow}$ denotes the Fourier transform operation.

2.1.2 Transforms of Selected Functions

Within this framework, the transform properties of several functions are of interest. The first of these is the Gaussian function:

$$\mathrm{Gaus}(x) = e^{-\pi x^2}. \tag{4}$$

The Gaussian is one of several functions which are invariant under Gaskill's transform:

$$\mathrm{Gaus}(x) \stackrel{\mathcal{F}}{\Longrightarrow} \mathrm{Gaus}(\xi). \tag{5}$$

We can use a limiting version of this function in our study of the properties of the impulse function, also commonly known as the Dirac delta function.* The properties of the Dirac delta function flow from the defining equation

$$\int_0^\infty f(y)\,\delta(y-x)\,dy = f(x) \tag{6}$$

for suitably smooth functions $f(x)$. This definition is also referred to as the delta function sifting property. We can study the Fourier transform properties of a delta function using a limiting form of the Gaussian function in combination with the dilation properties noted in equation (3). The delta function can be written as

$$\delta(x) = \lim_{a\to 0} \frac{1}{|a|}\,\mathrm{Gaus}\left(\frac{x}{a}\right). \tag{7}$$

The area under the function on the right-hand side (RHS) of equation (7) is unity for all nonzero a. Integration of this function times $f(x)$, as in equation (6), yields an approximation of $f(0)$ which improves as $a \to 0$. In the limit, this result is written using the notation in equation (6); however, strictly speaking, the limit cannot pass through the integral operation, as equation (7) does not satisfy the condition of bounded convergence (see the previous footnote). One way to think of the delta function in practical terms is as a sampling function whose operation is extremely rapid when compared to the rate of variations of the sampled function $f(x)$.

The delta function also features a scaling property such that

$$\delta\left(\frac{x-x_0}{a}\right) = |a|\,\delta(x-x_0). \tag{8}$$

Finally, based on the dilation rule (equation (3)), we can transform the delta function as

$$\delta(x) \overset{\mathcal{F}}{\Longrightarrow} \lim_{a\to 0} \mathrm{Gaus}(ax) = 1. \tag{9}$$

The δ function and its properties are necessary to understand the various features and properties of Gaskill's "comb" function:

$$\mathrm{comb}\left(\frac{x-x_0}{a}\right) \equiv |a| \sum_{n=-\infty}^{\infty} \delta(x-x_0-na). \tag{10}$$

* A rigorous treatment of the delta function involves the use of generalized functions (Kolmogorov and Fomin, 1970). The approach taken here views equation (6) as a notation representing the linear functional $L_x(f) = f(x)$ rather than an actual integral.

The name for this function (characteristic of other Gaskill function names) evokes its visual appearance. In this case, the comb consists of an infinite series of delta "tines" occurring at separation intervals $|a|$ along the x axis.

The comb function is also invariant under Fourier transformation:

$$\mathrm{comb}(x) \stackrel{\mathcal{F}}{\Longrightarrow} \mathrm{comb}(\xi). \tag{11}$$

Gaskill's (1978) discussion of this relation is rather detailed (pp. 205-206) and will not be repeated here. In it, Gaskill admits to ignoring "the Dirichlet condition that prohibits impulsive behavior in the function to be expanded." The result is thus not a rigorous proof, but can be made so using careful application of the theory of generalized functions (Kolmogorov and Fomin, 1970).

Using the comb function, a uniformly spaced sequence of delta functions will have a particularly simple form in frequency space:

$$\sum_{n=-\infty}^{\infty} \delta(x - na) = \frac{1}{|a|} \mathrm{comb}\left(\frac{x}{a}\right) \stackrel{\mathcal{F}}{\Longrightarrow} \mathrm{comb}(a\xi). \tag{12}$$

2.1.3 Convolution and Cross Correlation Operations

Given the form of the Fourier transform we see immediately that multiplication of a function by a constant scales the Fourier transform of the resulting product by the same constant. We have already considered dilated and shifted functions in the previous section. However, there are two other linear operations of particular interest which have unique Fourier transform properties. These are the convolution and cross correlation operations.

For two square integrable functions, $f(x)$ and $g(x)$, defined over the x axis, we define the convolution operation as

$$f(x) * g(x) = \int_{-\infty}^{\infty} f(a)\, g(x - a)\, da. \tag{13}$$

For the cross correlation operation we write

$$f(x) \star g(x) = \int_{-\infty}^{\infty} f(a + x)\, g(a)\, da = \int_{-\infty}^{\infty} f(a)\, g(a - x)\, da. \tag{14}$$

Gaskill notes (equation (6.11)) that while $f(x) * g(x) = g(x) * f(x)$, the cross correlation operation does not commute (equations (6.46) and (6.48)):

$$f(x) \star g(x) = f(x) * g(-x) \neq g(x) * f(-x) = g(x) \star f(x). \tag{15}$$

Under Fourier transform (Gaskill's Table 7.2) these operations considerably simplify:

$$\begin{aligned} f(x) * g(x) &\overset{\mathcal{F}}{\Longrightarrow} F(\xi)\, G(\xi); \\ f(x) \star g(x) &\overset{\mathcal{F}}{\Longrightarrow} F(\xi)\, G(-\xi). \end{aligned} \tag{16}$$

On the other hand, products of functions transform as

$$\begin{aligned} f(x)\, g(x) &\overset{\mathcal{F}}{\Longrightarrow} F(\xi) * G(\xi); \\ f(x)\, g(-x) &\overset{\mathcal{F}}{\Longrightarrow} F(\xi) \star G(\xi). \end{aligned} \tag{17}$$

2.1.4 Extension of Gaskill's Methods

Gaskill extends his one-dimensional analysis to two dimensions in order to use this theory in Fourier optics applications. We can extend these results to three dimensions in a similar manner. For example, a three dimensional version of the delta function becomes

$$\delta(x,\, y,\, z) = \delta(x)\, \delta(y)\, \delta(z), \tag{18}$$

Similar extensions exist for other one-dimensional functions.

A final feature of note is a consideration of the units by which the original functions are represented versus the units of the transformed functions. As we shall see, the units associated with series coefficients in the Fourier series representation of a function are the same units as the original function, whereas the units of the transform of a function $f(x)$ consist of the product of the original units of $f(x)$ times the units associated with the variable x. Integration with respect to the variable ξ, whose units are the inverse of x, removes this dependence during the inverse transform process.

2.2 The Fourier Series

In the representation of periodic functions, $p(x)$, a Fourier series is usually employed. Consider a real-valued function, $p(x)$, which is periodic over intervals of length X:

$$p(x) = p(x + mX), \tag{19}$$

where m is any integer.

2.2.1 *Transform Definition*

Let the Fourier series representation of this function be given by

$$p(x) = a_0 + 2\sum_{l=1}^{\infty}\left[a_l \cos\left(\frac{2\pi x l}{X}\right) + b_l \sin\left(\frac{2\pi x l}{X}\right)\right]. \tag{20}$$

This form was chosen to closely track Gaskill's Fourier method. Based on orthogonality relations among trigonometric functions, we can evaluate the coefficients a_l and b_l as

$$a_l = \frac{1}{X}\int_{-X/2}^{X/2} p(x)\cos\left(\frac{2\pi x l}{X}\right)dx; \tag{21}$$

$$b_l = \frac{1}{X}\int_{-X/2}^{X/2} p(x)\sin\left(\frac{2\pi x l}{X}\right)dx. \tag{22}$$

We choose the region of integration symmetrically about the origin for reasons that will become clear later in the discussion.

The factor 2 appearing in front of the summation in equation (20) can be removed by translating these results into complex form using Euler's formula:

$$e^{i\theta} = \cos(\theta) + i\,\sin(\theta), \qquad e^{-i\theta} = \cos(\theta) - i\,\sin(\theta), \tag{23}$$

where i is the imaginary root, $i = \sqrt{-1}$. Rearranging, we have,

$$\cos(\theta) = \frac{e^{i\theta} + e^{-i\theta}}{2}, \qquad \sin(\theta) = \frac{e^{i\theta} - e^{-i\theta}}{2\,i}. \tag{24}$$

The introduction of this formula into equation (20) leads to the complex form of the Fourier series, with the terms

$$2\left[a_l \cos\left(2\pi x \xi_l\right) + b_l \sin\left(2\pi x \xi_l\right)\right] = \tilde{P}_l\, e^{i2\pi x \xi_l} + \tilde{P}_l^*\, e^{-i2\pi x \xi_l}, \tag{25}$$

where $\xi_l = l/X$ and

$$\tilde{P}_l = a_l - i\,b_l; \qquad \tilde{P}_l^* = a_l + i\,b_l. \tag{26}$$

A superscripted asterisk denotes the complex conjugate operation.

The complex form of the Fourier series is then

$$p(x) = \sum_{l=-\infty}^{\infty} \tilde{P}_l \exp\left(i2\pi\xi_l x\right), \tag{27}$$

$$\tilde{P}_l = \frac{1}{X}\int_{-X/2}^{X/2} p(x)\exp\left(-i2\pi\xi_l x\right)dx. \tag{28}$$

Because $p(x)$ is a real-valued function, the coefficients $\tilde{P}_l$ obey the Hermitian property ($\tilde{P}_{-l} = \tilde{P}_l^*$), as may be inferred from equations (25) and (26) above.

2.2.2 Fourier Series Convolution and Cross Correlation

Two important related operations involving the Fourier series are again convolution and cross correlation. For the convolution operation we write

$$c(x) = f(x) * g(x) = \frac{1}{X} \int_{-X/2}^{X/2} f(x')\, g(x - x')\, dx'. \tag{29}$$

The cross correlation operation is given by

$$q(x) = f(x) \star g(x) = \frac{1}{X} \int_{-X/2}^{X/2} f(x' + x)\, g(x')\, dx'. \tag{30}$$

This function becomes an autocorrelation if $g(x)$ is replaced by $f(x)$. Notice that these operations avoid introducing the units of x into the resulting function, unlike the continuous versions in equations (13) and (14).

We are interested in how these two functions transform: Assume $f(x)$ has a Fourier series with coefficients $\tilde{F}_l$, and $g(x)$ has a series with coefficients $\tilde{G}_l$. We represent the Fourier transform of the cross correlation by a Fourier series with coefficients $\tilde{Q}_l$:

$$\begin{aligned} \tilde{Q}_l &= \frac{1}{X} \int_{-X/2}^{X/2} q(x)\, \exp\left(-i2\pi\, x\, \xi_l\right)\, dx \\ &= \frac{1}{X} \int_{-X/2}^{X/2} \left[\frac{1}{X} \int_{-X/2}^{X/2} f(x' + x)\, g(x')\, dx' \right] \exp\left(-i2\pi\, x\, \xi_l\right)\, dx. \end{aligned} \tag{31}$$

Multiplying by $1 = \exp\left(i2\pi\, x'\, \xi_l\right) \exp\left(-i2\pi\, x'\, \xi_l\right)$, the order of integration can be reversed, and a new variable $x'' = x' + x$ defined. Holding x' constant in the outer integral, we wish to integrate over x in the inner integral. Since x' is constant, $dx \rightarrow dx''$ and we may integrate the inner integral in terms of x'', leading to

$$\tilde{Q}_l = \frac{1}{X} \int_{-X/2}^{X/2} g(x') \left[\frac{1}{X} \int_{-X/2}^{X/2} f(x'')\, \exp\left(-i2\pi x''\xi_l\right)\, dx'' \right] \exp\left(i2\pi x'\xi_l\right)\, dx'. \tag{32}$$

The inner integral may then be evaluated to the constant $\tilde{F}_l$, which can then be factored out of the remaining integral.

$$\tilde{Q}_l = \tilde{F}_l \left[\frac{1}{X} \int_{-X/2}^{X/2} g(x')\, \exp\left(i2\pi\, x'\, \xi_l\right)\, dx' \right] = \tilde{F}_l\, \tilde{G}_{-l} = \tilde{F}_l\, \tilde{G}_l^*. \tag{33}$$

In the case of an autocorrelation, note that $\tilde{F}_l \, \tilde{F}_l^* = \left| \tilde{F}_l \right|^2$ is nonnegative.

The procedure for evaluating convolution series coefficients, $\tilde{C}_l$, is similar and results in series elements

$$\tilde{C}_l = \tilde{F}_l \, \tilde{G}_l. \tag{34}$$

These forms are relatively close to Gaskill's results given in equation (16). There, the transform of the convolution equalled the product of the individual transforms. Here, the convolution coefficients consist of products of pairs of appropriate coefficients of the individual transforms.

Let us now consider the extension of these results to three dimensions. Define the form of a transform for the function $f(x, y, z)$ as

$$f(\vec{s}) = \sum_{l=-\infty}^{\infty} \sum_{m=-\infty}^{\infty} \sum_{n=-\infty}^{\infty} \tilde{F}_{l,m,n} \exp\left(i \, 2\pi \, \vec{s} \cdot \vec{\xi}_{l,m,n} \right). \tag{35}$$

The Fourier series coefficients are evaluated via

$$\tilde{F}_{l,m,n} = \frac{1}{XYZ} \int_{-X/2}^{X/2} dx \int_{-Y/2}^{Y/2} dy \int_{-Z/2}^{Z/2} dz \, f(\vec{s}) \exp\left(-i \, 2\pi \, \vec{s} \cdot \vec{\xi}_{l,m,n} \right), \tag{36}$$

where the two vectors are given by

$$\vec{s} = x\hat{\imath} +, y\hat{\jmath} + z\hat{k}, \qquad \vec{\xi}_{l,m,n} = \frac{l}{X}\hat{\imath} + \frac{m}{Y}\hat{\jmath} + \frac{n}{Z}\hat{k}, \tag{37}$$

where $\hat{\imath}$, $\hat{\jmath}$, and $\hat{k}$ are unit vectors oriented along the x, y, and z axes, respectively. The dot product operation inside the exponentials is thus shorthand for

$$\vec{s} \cdot \vec{\xi}_{l,m,n} = \frac{lx}{X} + \frac{my}{Y} + \frac{nz}{Z}. \tag{38}$$

Since the functions we will be considering will be real-valued, the resulting three-dimensional array of points $\tilde{F}_{l,m,n}$ will exhibit a three-dimensional Hermitian property:

$$\tilde{F}_{-l,-m,-n} = \tilde{F}^*_{l,m,n}. \tag{39}$$

Also, when the signs associated with the subscripted indices are not specifically indicated, it will be expedient to write

$$\tilde{F}_{l,m,n} \longrightarrow \tilde{F}_{lmn}, \qquad \vec{\xi}_{l,m,n} \longrightarrow \vec{\xi}_{lmn}, \qquad \text{etc.} \tag{40}$$

We may imagine that the Fourier series coefficients $\tilde{F}_{lmn}$ are associated with specific points, $\vec{\xi}_{lmn}$, in a frequency space denoted by general vectors $\vec{\xi}$. As the size of the periodic volume $V = XYZ$ expands, volume dimensions X,

Y, and Z expand, resulting in closer spacing of the sample points within the frequency space. There are obvious advantages to closer spacings of points as this enhances the resolution of the transformed function. As the number of sample points increases, the magnitude of each sample point simultaneously decreases according to the factor $1/V = 1/(XYZ)$. The decreasing magnitude of individual sample points is thus exactly compensated by the increasing density of sample points.

2.2.3 Transforms of Periodic Functions

In studying the connection between Gaskill's Fourier transform methodology and the Fourier series representations just discussed, we now consider how Gaskill's Fourier methods handle periodic functions. To begin this discussion, consider the Fourier transform of a smoothly varying function, $f(x)$, convolved with a delta function. From the rules derived in section 2.1 we have

$$\delta(x) * f(x) \overset{\mathcal{F}}{\Longrightarrow} 1 \times F(\xi) = F(\xi). \tag{41}$$

Thus, the delta function acts as the identity operator of the convolution operation, just as zero is the identity operator under addition and one is the identity operator of multiplication.

Consider then, the convolution of $f(x)$ with an offset δ function:

$$\delta(x - x_0) * f(x) \overset{\mathcal{F}}{\Longrightarrow} \exp\left(-i\,2\pi\,x_0\,\xi\right)\, F(\xi) \overset{\mathcal{F}^{-1}}{\Longrightarrow} f(x - x_0). \tag{42}$$

We find, then, that convolution of $f(x)$ with the offset delta function is equivalent to positionally shifting the original function $f(x)$ by the distance x_0. For suitable functions $f(x)$, satisfying

$$\int_a^b |f(x)|\,dx < \infty, \quad |f(x)| < \infty, \tag{43}$$

where a and b are limits such that $f(x) = 0$ for $x < a$ and $x > b$, we then find the convolution of $f(x)$ with an appropriately scaled version of Gaskill's comb function yields the periodic function, $p(x)$,

$$p(x) = p(x + X) = f(x) * \frac{1}{X}\,\mathrm{comb}\left(\frac{x}{X}\right). \tag{44}$$

For the sake of simplicity let us assume that $f(x) = 0$ for all $|x| \geq X/2$.* Thus individual copies of $f(x)$ spawned by the convolution with the comb function will not spatially overlap.

---

* Technically, a and b could occupy any interval along the real axis and we need not have $b - a < X$. The simplifications involves establishing symmetric limits for a and b about the origin.

From equation (16), we can see that $p(x)$ Fourier transforms into

$$f(x) * \frac{1}{X}\,\mathrm{comb}\left(\frac{x}{X}\right) \stackrel{\mathcal{F}}{\Longrightarrow} F(\xi)\,\mathrm{comb}(X\xi). \tag{45}$$

Using the definition of the comb function, we may then write

$$p(x) \stackrel{\mathcal{F}}{\Longrightarrow} P(\xi) = \frac{F(\xi)}{X} \sum_{l=-\infty}^{\infty} \delta\left(\xi - \frac{l}{X}\right). \tag{46}$$

Note that while $F(\xi)$ was defined at all frequencies, the function $P(\xi)$ is only nonzero at unique frequencies, separated by intervals $\Delta\xi = 1/X$. Further note that because $f(x)$ equals zero outside the bounded region $-X/2 < x < X/2$, we may rewrite the integral for $F(\xi)$ as

$$F(\xi) = \int_{-\infty}^{\infty} f(x)\,\exp(-i\,2\pi\,x\,\xi)\,dx = \int_{-X/2}^{X/2} f(x)\,\exp(-i\,2\pi\,x\,\xi)\,dx. \tag{47}$$

Comparison between this result and equation (28) reveals a correspondence between the Fourier transform representation of a periodic function using Gaskill's Fourier transform, and the Fourier series representation described in section 2.1. The two transforms are related through the equation

$$\tilde{P}_l = \frac{F(l/X)}{X}. \tag{48}$$

This can be shown by deriving a formula for $p(x)$ starting with Gaskill's inverse transform:

$$\begin{aligned} p(x) &= \int_{-\infty}^{\infty} P(\xi)\,\exp\left(i\,2\pi\,x\,\xi\right)\,d\xi \\ &= \sum_{l=-\infty}^{\infty} \int_{-\infty}^{\infty} \frac{F(\xi)}{X}\,\delta\left(\xi - \frac{l}{X}\right)\,\exp\left(i\,2\pi\,x\,\xi\right)\,d\xi \\ &= \sum_{l=-\infty}^{\infty} \frac{F(l/X)}{X}\,\exp\left(i\,2\pi\,x\,\frac{l}{X}\right) \\ &= \sum_{l=-\infty}^{\infty} \frac{F(\xi_l)}{X}\,\exp\left(i\,2\pi\,x\,\xi_l\right). \end{aligned} \tag{49}$$

The final form of this equation corresponds to the complex form of the Fourier series (equation (27)) using the translation law contained in equation (48) above. We thus have a direct method of comparison and inter-transformation between two different Fourier methods for periodic functions.

This is a key result–the Fourier series is merely a representation of the Fourier transform when considering periodic functions.

2.3 The Fast Fourier Transform

The FFT is simply a method of calculating a discrete Fourier transform that uses a series of acceleration techniques originally developed by Danielson and Runga that were later popularized by Cooley and Tukey (cf. Ludeman, 1986). Ludeman's treatment of this technique is rather thorough and is followed closely in this text. Another standard treatment is found in Press et al. (1992), but involves a different sign in the complex argument. Regardless of the treatment, the key feature of the FFT is that a method has been found whereby the number of complex multiplications required to transform a data set can be significantly reduced by processing the data in a specific series of stages. The amount of time savings is proportional to the data set size: The FFT process requires on the order of $N \ln N$ complex multiplications compared to N^2 such multiplications for a straightforward discrete Fourier transform. As a result of this reduction, nearly all transform calculations performed digitally utilize the FFT procedure.

The reason for our present interest lies in standard descriptions of refractive turbulence, which are always in the form of a power spectrum (a Fourier frequency domain representation). These spectra form components of functions (described in sections 4.3 and 4.4), which must be inverse transformed using the FFT. Difficulties arise when one attempts to translate the power spectrum into a digital representation compatible with the FFT. This section lays the groundwork for that translation task.

The FFT process itself is a fast version of a discrete Fourier transform. And the discrete Fourier transform is simply a band-limited version of a Fourier series. The reason for the band limit is due to the finite number of samples in a digital data set. We let N be the number of samples of data in our data set. These samples are normally assumed to be point measurements separated from one another by some interval Δx. In our case we are interested in spatially separated data so Δx has dimensions of distance. Because the FFT is related to the Fourier series method, it is assumed that the data is periodic. The period used is $X = N\,\Delta x$.

For compatibility with the Fourier transform and series definitions, let us assume that the N samples are centered around an index value of zero, corresponding to the point $x = 0$. Numerically these points are assigned indices starting at $-N/2 + 1$ and continuing through index $N/2$. Call the index variable n, and assume that each of the N samples is a measurement of some underlying physical process, $f(x)$. Let us call the nth sample of this process $\hat{f}(n)$, corresponding to the value of $f(x)$ at location $x = n\,\Delta x$. Assume for the moment that this sample is taken instantaneously.

We should then be able to approximate the computation of a Fourier series coefficient (equation (28) via the following process:

$$\begin{aligned}
\tilde{F}_l &= \frac{1}{X} \int_{-X/2}^{X/2} f(x)\, \exp\left[-i2\pi\xi_l x\right]\, dx \\
&\approx \frac{1}{X} \sum_{n=-N/2+1}^{N/2} \hat{f}(n)\, \exp\left[-i2\pi\, l\Delta\xi\, n\Delta x\right]\, \Delta x \\
&= \frac{1}{X} \sum_{n=-N/2+1}^{N/2} \hat{f}(n)\, \exp\left[-i2\pi\, l\, \frac{1}{X}\, n\, \frac{X}{N}\right]\, \frac{X}{N} \\
&= \frac{1}{N} \sum_{n=-N/2+1}^{N/2} \hat{f}(n)\, \exp\left[-i\frac{2\pi\, l\, n}{N}\right] \\
&= \hat{F}(l).
\end{aligned} \tag{50}$$

Here, the integration over the x interval has been approximated using a step interval $\Delta x = X/N$ and assuming that the sample value approximately represents the value of $f(x)$ over each interval.

We used a change of notation, referring to the approximations using the symbology $\hat{F}(l)$, because the sampled versions are qualitatively different from their continuous cousins. For one, the last form of the computational equation involves the quantity $2\pi\, l\, n/N$ in the exponent. The computation of the $\hat{F}(l)$ coefficients has thus lost all connection to the period length X dependence. Hence it is necessary to do external book keeping to keep track of the relationship between the indexed frequency results and their physical meanings. Further, because the data are no longer continuous, unlike the Fourier series coefficients, the series of $\hat{F}(l)$ coefficients only have N unique values. We can see this by looking at frequency coefficient $\hat{F}(l+N)$. We find that it has the same value as coefficient $\hat{F}(l)$. This is because

$$\begin{aligned}
\exp\left[-i\left(\frac{2\pi\,(N+l)\,n}{N}\right)\right] &= \exp\left[-i\,(2\pi\,n)\right]\, \exp\left[-i\left(\frac{2\pi\, l\, n}{N}\right)\right] \\
&= \exp\left[-i\left(\frac{2\pi\, l\, n}{N}\right)\right],
\end{aligned} \tag{51}$$

since $\exp[-i\,2\pi\,n] = 1$ for any n. One may therefore attempt to calculate as many spectral coefficients as desired, but only the first N values will be unique. All others will be periodic duplicates of the first N results.

We may simplify our writing of the transform operation by the introduction of the so-called "twiddle" factors, W_N^{nl}:

$$\hat{F}(l) = \frac{1}{N} \sum_{n=-N/2+1}^{N/2} \hat{f}(n)\, W_N^{nl}, \qquad l = -N/2+1, ..., N/2; \tag{52}$$

where

$$W_N = \exp\left(-i\,2\pi/N\right), \qquad W_N^{nl} = \exp\left(-i\,\frac{2\pi nl}{N}\right). \tag{53}$$

The range of l values has also been chosen symmetrically about the origin $l = 0$.

We now show that the inverse FFT process is given by

$$\hat{f}(n) = \sum_{l=-N/2+1}^{N/2} \hat{F}(l)\, W_N^{-nl}, \qquad n = -N/2+1, ..., N/2. \tag{54}$$

This relationship can be ascertained as correct by substituting the definition of $\hat{F}(l)$ into the equation for $\hat{f}(n)$:

$$\begin{aligned}
\hat{f}(n) &= \sum_l \hat{F}(l)\, \exp\left(i\frac{2\pi nl}{N}\right), \\
&= \sum_l \left[\frac{1}{N}\sum_{n'} \hat{f}(n')\, \exp\left(-i\frac{2\pi n' l}{N}\right)\right] \exp\left(i\frac{2\pi nl}{N}\right), \\
&= \sum_{n'} \frac{\hat{f}(n')}{N} \sum_l \exp\left[i\,\frac{2\pi\, l\,(n-n')}{N}\right].
\end{aligned} \tag{55}$$

Due to the orthogonality between different elements of the complex inner summation,

$$\sum_{l=-N/2+1}^{N/2} \exp\left[i\,\frac{2\pi\, l\,(n-n')}{N}\right] = N\,\delta_n^{n'}, \tag{56}$$

where,

$$\delta_l^m = \begin{cases} 1, & l = m; \\ 0, & l \neq m. \end{cases} \tag{57}$$

Here, δ_l^m is the Kronecker delta function with l and m integer arguments. In effect, equations (56) and (57) are the mathematical expressions of a geometrical argument. The N components of the summation in equation (56) represent the N complex roots of the equation $x^N = 1$. These roots are arranged symmetrically about the origin in the complex plane. When summed these roots cancel one another out in all but the case where $N = 0$.

Using the Kronecker delta notation we can rewrite the RHS of equation (55) as

$$\sum_{n'} \hat{f}(n')\,\delta_n^{n'} = \hat{f}(n), \quad \text{Q.E.D.} \tag{58}$$

Note that $\delta_n^{n'}$ has the same sifting properties with respect to summation that the Dirac delta function has with respect to integration.

There are, however, problems that arise with respect to the FFT. These primarily focus around the limited nature of the data set in terms of the number of samples, N, and the finite interval, Δx, between samples. Due to the limited number of samples and their assumed periodicity, using raw data one often encounters jump discontinuities at the ends of the data sets. To limit the amount of spurious noise that would be introduced to the spectra if this data was transformed in raw form, the data is nearly always "windowed" (Harris, 1978; Ludeman, 1986). The windowing process involves multiplying the data set by a function which tapers to zero at both ends, resulting in an imposed periodicity.

The second effect relates to the finite intervals Δx and X. Because of the finite number of samples, the minimum resolvable frequency is $1/X$ and that maximum unique frequency is $N/(2X) = 1/(2\,\Delta x)$, which is also referred to as the Nyquist frequency. Usually the Nyquist frequency is used to establish a requirement for low-pass filtering of the input analog signal to remove higher frequency content. Signals arriving with energy content at higher frequencies than the Nyquist frequency will be aliased into lower frequency portions of the computed spectrum.

In our problem, windowing is not necessarily a concern because we begin in the transformed domain and inverse transform to the real domain. The resulting real function is therefore guaranteed to be periodic. However, we must ensure that the size of the domain is sufficient to adequately characterize the turbulence structure, including outer scale effects at low frequencies and inner scale effects at high frequencies. Within the surface boundary layer, the length scales associated with turbulence extend from about an order of magnitude smaller than inner scales of several millimeters (Tofsted, 1991) to outer scales measuring up to dozens of meters (Tofsted, 2000). Means of handling these requirements are discussed in chapter 4 when considering generation of phase/deflector screens.

3. Optical Turbulence Structure

In chapter 2 we considered three related transform methods useful for describing real, periodic real, and sampled periodic real functions, respectively. We discovered that the Fourier transform can be related to the Fourier series of a periodic function through use of Dirac delta functions. We also discussed the similarity in form between the FFT and the Fourier series. However, we must now develop a connection between results contained in the optical turbulence literature and deflector propagation screens discussed in chapter 4.

Relating these two literature sources is not simple. The FFT method assumes the function being modeled is periodic over some fundamental volume V. Conversely, the optical turbulence literature generally derives results involving expectation values for aperiodic functions defined over all space. Hence, rigorous evaluation of expectation values would require an averaging operation evaluated over infinite volume.

To avoid confusion between the methods described in this chapter and those discussed in the previous chapter, we will use position vector $\vec{r}$ instead of $\vec{s}$. The primary quantity of interest in this analysis is the variable n, the refractive index in the earth's atmosphere. One very useful spatial structure property of n is the spatial covariance function, Γ_n, given by (Goodman, 1985)

$$\begin{aligned}\Gamma_n(\vec{r}_1, \vec{r}_2) &= \Big\langle \big[n(\vec{r}_1) - \langle n(\vec{r}_1)\rangle\big]\,\big[n(\vec{r}_2) - \langle n(\vec{r}_2)\rangle\big] \Big\rangle \\ &= \Big\langle n(\vec{r}_1)\, n(\vec{r}_2)\Big\rangle - \Big\langle n(\vec{r}_1)\Big\rangle\Big\langle n(\vec{r}_2)\Big\rangle,\end{aligned} \tag{59}$$

where angle brackets ($\langle\rangle$) represent expectation operations, and vectors $\vec{r}_1$ and $\vec{r}_2$ represent two positions in a presumably infinite medium.

Modeling the volume as infinite in size usually leads a homogeneity assumption which I now introduce. However, I make this approximation while recognizing that it has limitations and may need to be altered in the future. The problem is that homogeneous turbulence is not physically realizable (Hinze, 1987). Hinze then proceeds to considered the degree of damage caused by maintaining this assumption. Hinze's following commentary observes that, far from damaging, inhomogeneities are necessary to maintain the level of the turbulence itself. Due to dissipation at small scales, energy must be introduced at the large scales to maintain the energy cascade across the inertial subrange. When this energy is unavailable the turbulence level decays. Though a significant consideration from the point of view of models to describe the turbulence itself, the amount

of energy needed to maintain the cascade is not large compared to the energy maintained in the field itself, so the fractional error is relatively small.

Granted these problems with the homogeneous assumption, we nevertheless employ it to avoid major complications in the mathematical analysis. The homogeneous turbulence condition involves assuming that the mean refractive index is constant with position and that the structure of the turbulence is also constant with position. The first of these conditions can be stated mathematically as, $n_0 = \langle n(\vec{r}_1) \rangle = \langle n(\vec{r}_2) \rangle$ in equation (59).

The second condition states that Γ_n is dependent only on the vector difference $\vec{r}_2 - \vec{r}_1$:

$$\Gamma_n(\vec{r}_1, \vec{r}_2) = \Gamma_n(\vec{r}), \qquad \vec{r} = \vec{r}_2 - \vec{r}_1. \tag{60}$$

A further consequence of the homogeneity assumption follows when we parse the refractive index into its mean and fluctuating components:

$$n(x, y, z) = n_0 + n_1(x, y, z). \tag{61}$$

From the definition of the covariance in equation (59), as long as the mean refractive index is constant with position, we can write

$$\Gamma_n(\vec{r}) = \Big\langle n_1(\vec{r}_1)\, n_1(\vec{r}_1 + \vec{r}) \Big\rangle. \tag{62}$$

The covariance function Γ_n is thus an autocorrelation statistically averaged across all possible realizations of the $n_1(\vec{r})$ field.

Because of the homogeneity property of the n_1 field, and because its second order statistics are assumed uniform with position, we can show that

$$\Gamma_n(\vec{s}) = \frac{1}{XYZ} \left\langle \int_{-X/2}^{X/2} \int_{-Y/2}^{Y/2} \int_{-Z/2}^{Z/2} n_1(\vec{s}_1)\, n_1(\vec{s}_1 + \vec{s})\, d\vec{s}_1 \right\rangle, \tag{63}$$

where X, Y, and Z are the dimensions of a finite volume.

Following methods of stochastic integration discussed by Stark and Woods (1986) and categories of random processes such as discussed by Goodman (1985), as long as the n_1 field is strictly stationary up to fourth order joint probabilities, we may pass the expectation operators through the integration operators and obtain

$$\begin{aligned} &\left\langle \int_{-X/2}^{X/2} \int_{-Y/2}^{Y/2} \int_{-Z/2}^{Z/2} n_1(\vec{s}_1)\, n_1(\vec{s}_1 + \vec{s})\, d\vec{s}_1 \right\rangle \\ &\quad = \iiint \langle n_1(\vec{s}_1)\, n_1(\vec{s}_1 + \vec{s}) \rangle\, d\vec{s}_1 = \iiint \Gamma_n(\vec{s})\, d\vec{s}_1 \\ &\quad = \Gamma_n(\vec{s}) \iiint d\vec{s}_1 = XYZ\, \Gamma_n(\vec{s}). \end{aligned} \tag{64}$$

The XYZ volumes then cancel and equation (63) is shown to hold.

Let us now write the volume integration associated with equation (63) as

$$A(\vec{s}) = \int\int\int n_1(\vec{s}_1)\, n_1(\vec{s}_1 + \vec{s})\, d\vec{s}_1. \tag{65}$$

Rewriting the original equation, we have

$$\Gamma_n(\vec{s}) = \frac{\langle A(\vec{s}) \rangle}{XYZ}. \tag{66}$$

If it were possible to extend X, Y, and Z without limit, we note that $A(\vec{s})$ then appears as an autocorrelation function and we could Fourier transform A such that

$$A(\vec{s}) \overset{\mathcal{F}}{\Longrightarrow} \aleph(\vec{\xi}) = N_1(\vec{\xi})\, N_1(-\vec{\xi}). \tag{67}$$

$N_1(\vec{\xi})$ here would represent the Fourier transform of the $n_1(\vec{s})$ fluctuation field. Unit analysis reveals that $\aleph$ has units of volume squared (m^6) while N_1 has units of m^3.

Unfortunately, this procedure is not possible. The resulting integral definition for A would diverge for any non-zero value of $\Gamma_n(\vec{s})$ such that the ratio $\langle A(\vec{s}) \rangle / XYZ$ remained non-zero. Because of this limitation, the most direct method of simulating the effects of turbulence (by directly simulating the fluctuation field n_1 via its Fourier transform) is unavailable.

3.1 The Refractive Index Spectrum

It is in the homogeneous form that we normally find the relationship between the covariance and the refractive index power spectrum, Φ_n:

$$\Phi_n(\vec{\kappa}) = \left(\frac{1}{2\pi}\right)^3 \iiint_{-\infty}^{\infty} \Gamma_n(\vec{r})\, e^{i\vec{r}\cdot\vec{\kappa}}\, d\vec{r}. \tag{68}$$

This relationship has the form of a Fourier transform, but it is immediately obvious that it is not in the same form as equation (1). The difference is in the change of conventions between the standard used in the turbulence community and the standard used in writing the FFT and Gaskill's form for the Fourier transform. This discrepancy was a major reason for writing this report in the first place. To resolve these differences, we will develop the refractive index spectrum according to the standard methods used in the turbulence literature first, and then find the means of representing Φ_n in a form compatible with Gaskill's Fourier transform in section 3.3.

The quantity $\vec{\kappa}$ is called the spatial frequency vector. Its magnitude, the spatial frequency κ, is given in units of radians per meter. The refractive index

covariance can be recovered from the refractive index power spectrum through the inverse transform relationship

$$\Gamma_n(\vec{r}) = \iiint_{-\infty}^{\infty} \Phi_n(\vec{\kappa})\, e^{-i\vec{r}\cdot\vec{\kappa}}\, d\vec{\kappa}. \tag{69}$$

The power spectrum, Φ_n, is also often referred to in statistics literature as the characteristic function of Γ_n (Papoulis, 1984; Panofsky and Dutton, 1984).

As a further simplification, it is often assumed that the turbulence is isotropic. In this case only the magnitudes, r and κ, of vectors $\vec{r}$ and $\vec{\kappa}$, respectively, are significant. By integration over the angular variables in equations (68) and (69), these three-dimensional integrations can be simplified to the one-dimensional relations (cf. Beland, 1993):

$$\Phi_n(\kappa) = \left(\frac{1}{2\pi}\right)^3 \int_0^{\infty} \Gamma_n(r)\, \frac{\sin(r\kappa)}{r\kappa}\, 4\pi r^2\, dr; \tag{70}$$

$$\Gamma_n(r) = \int_0^{\infty} \Phi_n(\kappa)\, \frac{\sin(r\kappa)}{r\kappa}\, 4\pi\kappa^2\, d\kappa. \tag{71}$$

In Tofsted (2000) the properties of the outer-scale-influenced refractive index spectrum were described using the formula

$$\Phi_n(\kappa) = \beta_n\, C_n^2 \left[\frac{A_1\, (\mathcal{L}_a\,\kappa)^2\, \mathcal{L}_a^{11/3}}{\left[1 + (\mathcal{L}_a\,\kappa)^2\right]^{17/6}} + \frac{(1 - A_1)\, (\mathcal{L}_b\,\kappa)^4\, \mathcal{L}_b^{11/3}}{\left[1 + (\mathcal{L}_b\,\kappa)^2\right]^{23/6}} \right], \tag{72}$$

where C_n^2 is the refractive index structure parameter, having units of $\mathrm{m}^{-2/3}$; the constant A_1 was found to have the value 8.2; and $\mathcal{L}_a$ and $\mathcal{L}_b$ were found to be related to the outer scale through

$$\mathcal{L}_a = 2.0741\, L_o; \qquad \mathcal{L}_b = 2.4767\, L_o. \tag{73}$$

β_n is a constant of integration,

$$\beta_n = \frac{5}{36}\, \frac{2^{2/3}\,\Gamma(5/6)}{\pi^{3/2}\,\Gamma(2/3)} \approx 0.033, \tag{74}$$

where the Γ functions here refer to Euler's gamma function, defined by

$$\Gamma(x) = \int_0^{\infty} e^{-t}\, t^{x-1}\, dt, \quad x > 0, \tag{75}$$

such that $\Gamma(k+1) = k\,\Gamma(k) = k!$

This spectral form provides a more accurate model of the turbulence spectrum in the vicinity of the outer scale. Unlike the misnamed von Kármán spectrum, which approaches a nonzero constant value at zero frequency, this spectrum correctly approaches zero at $\kappa = 0$, consistent with von Kármán's original intent (Hinze, 1987; von Kármán, 1948).

3.1.1 Outer Scale Definition

In Tofsted (2000) I developed a more realistic refractive index spectrum based on data collected during the Kansas 1968 experiment. Based on that analysis I set the outer scale, L_o, based on the point at which the knee of the new spectrum significantly departs from the standard Kolmogorov spectrum (Kolmogorov, 1962), symbolized by Φ_{nK}. To identify this point, let $\kappa_\oslash = 1/L_o$ equal the frequency associated with the outer scale. Then define the outer scale as that point in the spectrum, where

$$\Phi_n(\kappa_\oslash) = \frac{1}{2}\,\Phi_{nK}(\kappa_\oslash). \tag{76}$$

The Kolmogorov spectrum is given by the form

$$\Phi_{nK}(\kappa) = \beta_n\, C_n^2\, \kappa^{-11/3}. \tag{77}$$

This form assumes both an infinite outer scale length and an inner scale length of zero. Hence, the Kolmogorov spectrum is applicable for the inertial subrange portion of the spectrum, and this is normally how it is calculated, but in practical applications involving integrations over the entire spectrum this caveat is usually ignored.

3.1.2 Covariance Evaluation

We can explicitly evaluate the covariance function $\Gamma_n(r)$ for the outer-scale-influenced spectrum through direct integration. From the form given for $\Phi_n(\kappa)$ in equation (72), it is expedient to identify two functions

$$G_1(r_a) = 4\pi \int_0^\infty \frac{\kappa_a^4}{(1+\kappa_a^2)^{17/6}}\,\frac{\sin(r_a\,\kappa_a)}{r_a\,\kappa_a}\,d\kappa_a, \tag{78}$$

$$G_2(r_b) = 4\pi \int_0^\infty \frac{\kappa_b^6}{(1+\kappa_b^2)^{23/6}}\,\frac{\sin(r_b\,\kappa_b)}{r_b\,\kappa_b}\,d\kappa_b, \tag{79}$$

where $r_a = r/\mathcal{L}_a$, $\kappa_a = \kappa\,\mathcal{L}_a$, $r_b = r/\mathcal{L}_b$, and $\kappa_b = \kappa\,\mathcal{L}_b$.

To solve for functions G_1 and G_2, one could use integration by parts. The term $\kappa\,d\kappa/(1+\kappa^2)^\nu$ can be integrated directly, through the change of variables $x = 1+\kappa^2$. By this approach the exponent of the κ term in the numerator is reduced. The resulting terms can then be integrated using Gradshteyn and Ryzhik's (1980) forms 3.771.2 and 3.771.5. Waterloo's Maple 6 software was used to initially evaluate these integrals. These results were then simplified by combining I-type Bessel functions to produce K-type Bessel functions:

$$G_1(r_a) = \frac{\pi^{3/2}\,r_a^{1/3}}{2^{1/3}\,\Gamma(17/6)}\,\left[3\,K_{1/3}(r_a) - r_a\,K_{2/3}(r_a)\right]; \tag{80}$$

$$G_2(r_b) = \frac{\pi^{3/2} r_b^{1/3}}{17\, 2^{1/3}\, \Gamma(17/6)} \left[\left(3 r_b^2 + 45\right) K_{1/3}(r_b) - 26\, r_b\, K_{2/3}(r_b) \right]. \qquad (81)$$

Here, $\Gamma(r)$ is the gamma function of argument r, and $K_\alpha(r)$ is the modified Bessel function of the second kind of order α and argument r (cf. Kreyszig, 1972, pg. 134).

The covariance function can then be written

$$\Gamma_n(r) = \beta_n\, C_n^2 \left[A_1\, \mathcal{L}_a^{2/3}\, G_1\left(\frac{r}{\mathcal{L}_a}\right) + (1 - A_1)\, \mathcal{L}_b^{2/3}\, G_2\left(\frac{r}{\mathcal{L}_b}\right) \right]. \qquad (82)$$

3.2 The Refractive Index Structure Function

The behavior of the covariance function in equation (82) can be compared with the behavior of the Kolmogorov spectrum through the refractive index structure function, $D_n(\vec{r})$, defined as

$$D_n(\vec{r}) = \left\langle \left[n(\vec{s}) - n(\vec{s} + \vec{r}) \right]^2 \right\rangle. \qquad (83)$$

Application of the isotropic and homogeneity conditions reveals that D_n can be written as a function of $|\vec{r}|$ only. Then, $D_n(r)$ and $\Gamma_n(r)$ are shown to be related through

$$D_n(r) = 2\left[\Gamma_n(0) - \Gamma_n(r)\right]. \qquad (84)$$

The use of $D_n(r)$ rather than $\Gamma_n(r)$ permits comparison between the outer-scale-influenced spectrum and the Kolmogorov spectrum. Different covariance functions, $\Gamma_n(r)$, cannot be compared directly because the Kolmogorov spectrum yields a singularity at $\Gamma_n(0)$, indicating its overall variance is infinite. Nevertheless, Tatarski (1961) and Clifford (1978) showed that the structure function for the Kolmogorov spectrum can be evaluated directly from Φ_n without evaluating Γ_n first. Following this approach, one finds the Kolmogorov form of the structure function to be

$$D_{nK}(r) = C_n^2\, r^{2/3}. \qquad (85)$$

Normally this result is caveated such that only separation distances $\ell_o < r < L_o$ are considered valid. Similar restrictions are applied to the range of valid κ values in the Kolmogorov spectrum itself. For example, Tatarski (1961) assigns κ_0 and κ_m, referring to outer and inner scale limits such that $\kappa_0 < \kappa < \kappa_m$. These spectral limits define the bounds of the so-called inertial subrange. However, as mentioned in section 3.1.1, the entire spectrum ($0 \leq \kappa \leq \infty$) is often integrated when evaluating the effects of the Kolmogorov spectrum in various propagation calculations. It is for this reason that when considering the Kolmogorov spectrum in the remainder of this document, I have chosen

to impose the full consequences corresponding to use of the entire Kolmogorov spectrum to highlight the deleterious effects.

The first of these effects can be seen when comparing plots of structure functions based on the outer-scale-influenced and Kolmogorov spectra, $D_n(r)$ and $D_{nK}(r)$ respectively, in figure 1. For small separation distances $r \ll L_o$, $D_n(r)$ and $D_{nK}(r)$ are approximately equal. As r exceeds L_o the outer scale limited structure function levels off to a finite maximum value $2\Gamma_n(0)$. Using the complete Kolmogorov spectrum, we find that $\Gamma_{nK}(0) = \infty$. Hence, the Kolmogorov structure function increases without limit with increasing separation distance r.

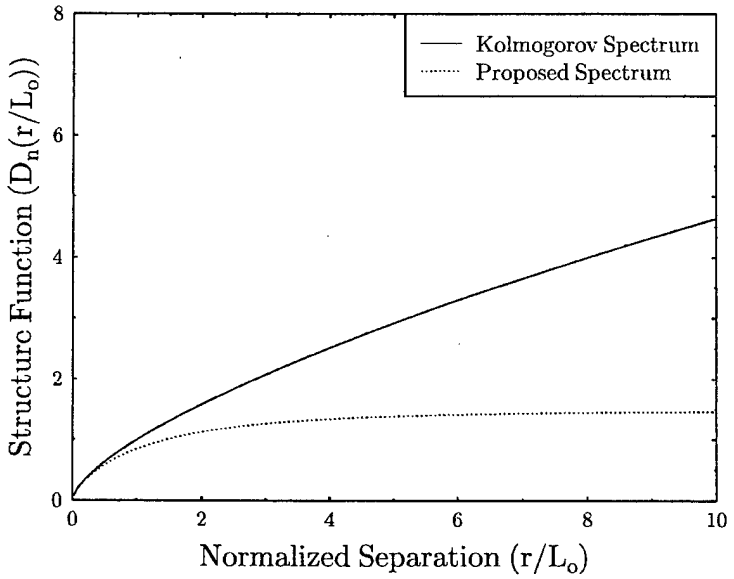

Figure 1. Comparison between Kolmogorov and outer-scale-influenced structure functions.

As illustrated in figure 2, as the size of the outer scale increases, so does the asymptotic limit of $D_n(r)$, providing a close approximation between the Kolmogorov D_{nK} function and the outer-scale-influenced D_n function for longer separation distances. This figure also indicates that the rise distance required for $D_n(r)$ to reach some fixed percentage of its asymptotic value is also longer as L_o increases. To adequately model correlation effects in a propagation simulation, one must contain nearly all this variation within the fundamental volume V of the modeled region. Since the rise distance increases with increasing L_o, it naturally implies that large L_o requires larger modeled volumes to adequately simulate the influences of the outer scale in such propagation situations.

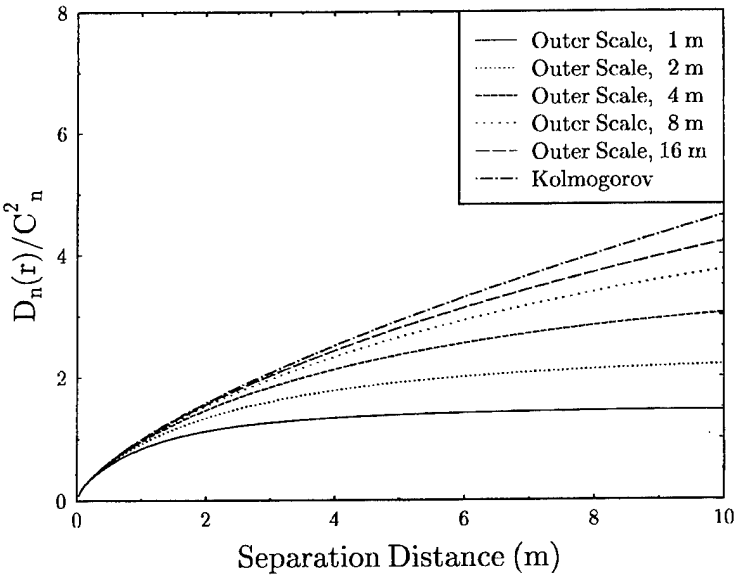

Figure 2. Comparison between different outer-scale-influenced structure functions with varying outer scale lengths.

3.3 Transforming the Covariance Function

We are now in a position to compare the Fourier-like characteristic functions used in the standard turbulence theory with the Fourier methods discussed in chapter 2. Due to the difference in form between the standard form of presentation of the spectrum as opposed to its means of implementation in the standard form for the FFT, it is necessary to make a transformation between the two forms. In particular, we need to compare the transformation pair

$$\Phi_n(\vec{\kappa}) = \left(\frac{1}{2\pi}\right)^3 \iiint_{-\infty}^{\infty} \Gamma_n(\vec{r})\, e^{i\vec{r}\cdot\vec{\kappa}}\, d\vec{r}, \tag{86}$$

$$\Gamma_n(\vec{r}) = \iiint_{-\infty}^{\infty} \Phi_n(\vec{\kappa})\, e^{-i\vec{r}\cdot\vec{\kappa}}\, d\vec{\kappa}, \tag{87}$$

which we simplified to

$$\Phi_n(\kappa) = \left(\frac{1}{2\pi}\right)^3 \int_0^{\infty} \Gamma_n(r)\, \frac{\sin(r\kappa)}{r\kappa}\, 4\pi r^2\, dr, \tag{88}$$

$$\Gamma_n(r) = \int_0^{\infty} \Phi_n(\kappa)\, \frac{\sin(r\kappa)}{r\kappa}\, 4\pi\kappa^2\, d\kappa, \tag{89}$$

with the transformation pair

$$\Psi_n\left(\vec{\xi}\right) = \iiint_{-\infty}^{\infty} \Gamma_n\left(\vec{s}\right) e^{-i\,2\pi\,\vec{s}\cdot\vec{\xi}}\, d\vec{s}, \tag{90}$$

$$\Gamma_n\left(\vec{s}\right) = \iiint_{-\infty}^{\infty} \Psi_n\left(\vec{\xi}\right) e^{i\,2\pi\,\vec{s}\cdot\vec{\xi}}\, d\vec{\xi}, \tag{91}$$

which we would use if basing our methods on the techniques used by Gaskill.

Previously, we have used $\vec{s}$ and $\vec{r}$ to denote spatial variables in the two different systems. What if these variables actually denote the same quantity? How then are functions Φ_n and Ψ_n related to one another?

Comparing the arguments in the exponentials, we must have $\vec{\kappa} = -2\pi\vec{\xi}$. We find, however, that the sign difference between these two variables is immaterial because both Φ_n and Ψ_n must be radially symmetric. Thus, the magnitudes of κ and ξ must be related as $\kappa = 2\pi\xi$. Making this substitution in equation (90), we find that Ψ_n is equal to the triple integral in equation (86), leading to a relation between Ψ_n and Φ_n:

$$\Psi_n(\xi) = (2\pi)^3\,\Phi_n(2\pi\xi). \tag{92}$$

In this form, the Ψ_n values are magnified by the $8\pi^3$ factor because in ξ space the Ψ_n function decays proportionally more rapidly compared to the Φ_n κ-space representation. The difference is in the units of cycles per meter in ξ space versus the radians per meter units in κ space. From a practical viewpoint these results allow us to avoid converting from Φ_n to Γ_n and then to Ψ_n. Instead, we can rescale directly from Φ_n to Ψ_n.

Having established the relationship between Ψ_n and Φ_n, we may also rewrite the spherically symmetric forms of the integral relations between $\Phi_n(\kappa)$ and $\Gamma_n(r)$ in terms of $\Psi_n(\xi)$ and $\Gamma_n(s)$:

$$\Psi_n(\xi) = \int_0^{\infty} \Gamma_n(s)\,\frac{\sin(2\pi s\xi)}{2\pi s\xi}\,4\pi\,s^2\,ds; \tag{93}$$

$$\Gamma_n(s) = \int_0^{\infty} \Psi_n(\xi)\,\frac{\sin(2\pi s\xi)}{2\pi s\xi}\,4\pi\,\xi^2\,d\xi. \tag{94}$$

This spherically symmetric transform pair are identical (except for a change of variables) for both forward and inverse transforms. These are thus the three-dimensional equivalent of the Hankel transform results given by Gaskill (1978, pg. 320) that were also self-reciprocal for forward and inverse transforms for cylindrically symmetric functions.

4. Deflector and Phase Screens

This chapter considers the use of the functions Γ_n and Ψ_n in generating what will be termed deflector and phase screens. These objects are usable in two different approaches to modeling propagation through optical turbulence: (1) Deflector screens are useful in describing the shape distorting effects of turbulence through a model of positionally varying tilt effects; (2) Phase screens model turbulence effects by distorting a phase front and propagating the distorted phase front between successive screens via diffraction limited propagation equations. This chapter describes both propagation methods in detail, though the focus is on the generation of the screens and deflector screens in particular.

As in chapters 2 and 3, gaps also exist in the phase screen literature, which are again addressed through the derivations. For example, a key assumption underlying the transformation from Fourier transform to Fourier series results is typically handled through reference to prior literature. But these references are to papers rather far afield of the current subject matter (e.g. Shinozuka and Jan, 1972; Borgman, 1969). Due to significant differences in nomenclature and symbology, comparison is difficult. Hence, a unified presentation is sought to restate results that are not available in standard references on this topic. Also, the derivation for deflector screens is completely new.

It should be noted here that the overarching goal of this research is to model the propagation of a scene (an undisturbed original image) through synthetic turbulence. The model for this propagation assumes a radiance pattern (the scene) is being emitted from a source region (the object plane) as incoherent radiation from a very large number of point sources. If no turbulence were present, the energy emitted from the object plane would propagate over a path of length Z to an imaging system of aperture diameter D and focal length f. The imaging system model consists of the single aperture, an objective lens, and an image plane where the received image is detected through some sort of quantized array. This array samples the image into regions called pixels (picture elements) of single-axis angular subtense ϕ_p radians each. Projecting backward through the system lens and over path length Z, each pixel in the image plane corresponds to energy emitted from a region of size $Z\phi_p$ by $Z\phi_p$ in the object plane. Even for very narrow field of view systems, each such source region must consist of a very large number of independent emitters, in support of the concept that the signal arises as an incoherent radiation field.

Based on this model, the remainder of this chapter describes how phase screens and deflector screens can permit the incorporation of turbulence effects to the

propagation scenario just described for diffraction limited optics. Section 4.1 provides an overview of diffraction and deflection propagation techniques. In section 4.2 an analysis is performed for light passing through a slab of atmosphere of thickness Δ. Perturbations in the crossing time for light entering the slab at different transverse positions can then be modeled in terms of crossing time correlation spectra described in section 4.3. These spectra are applied directly in the diffraction propagation approach. The deflection method relies on a further determination of beam deflection effects, as discussed in section 4.4.

4.1 Propagation Methodologies

As pointed out at the close of chapter 3, functions Γ_n and Ψ_n cannot be directly inverse transformed to generate a randomized volume-based n_1 function. If this were so, randomized n_1 fields could be generated via an inverse transform process. A propagation technique could then numerically propagate through this volume. As will be seen in sections 4.1.1 and 4.1.2, such propagation can be modeled in two fashions, the former based on geometric optics and the latter based on diffraction propagation.

The geometric optics approach represents an extension of the refractive raytracing methodology (Tofsted, 1989b) developed to study refractive path bending effects on tank gunnery. This method is akin to image modification techniques later developed to study the effects of mirages (cf. Lehn, 2000; Lehn et al., 1994; Lehn and Friesen, 1992; Sozou and Loizou, 1994) on image propagation. Both methods considered only vertically stratified atmospheres and only dealt with the mean refractive index structure. The development of deflector screens, which covers sections 4.2 through 4.4, extends these effects to three-dimensionally varying refractive index structures.

The development of the deflector screen approach is based in large part on the foundation of the phase screen method originally developed to study beam wave propagation through turbulence (cf. Martin and Flatté, 1988; Davis and Walter, 1994). The original developers of the phase screen method seem to be Fleck et al. (1975), but their published analysis contained errors. These errors later appeared unchanged in the open literature version of their report, Fleck et al. (1976). Regardless, in sections 4.2 and 4.3 a reanalysis of their results is given which correctly derives their equations.

In general the term screen implies a two-dimensional object. In effect the use of screens means that turbulence effects along the optical path are being concentrated into planes (or screens) of interaction. The term screen is used simply because a mesh of sample values is used instead of a continuous function of position. Both phase screens and deflector screens have these qualities in common, as their derivations are similar.

In this analysis we shall see the other ways in which the deflector and phase screen approaches are similar. However in its full form, the phase screen (diffraction propagation) approach should produce the same qualitative results

as the deflector screen (geometrical optics) approach while yielding more accurate results. The difference is computational cost. To be accurate, the phase screen approach may require orders of magnitude more computational time than the deflector screen approach, yet provide only marginally different results. As pointed out by Fried (1982), the majority of effects can be modeled using geometrical optics methods. Though potentially prohibitive, phase screen method results can be used in canonical cases to provide a check on the accuracy and circumscribe the region of applicability of the deflector screen approach.

4.1.1 Geometric Optics Approach

The geometric optics method is similar to the refractive raytracing calculations made by the EOSAEL (Electro-Optical Systems Atmospheric Effects Library) module REFRAC (Tofsted, 1987, 1989a, 1989b). This module was originally developed to study the effects on tank gun accuracy of vertical refractive index gradients caused by surface heating and cooling. Here, though, the technique is extended to include gradients of refractive index in both the vertical and horizontal directions.

Let us begin by defining the propagating radiation in terms of a small angle approximation. Under this approximation we assign the main direction of propagation as lying along the positive z axis. Let us identify a unit vector $\hat{\Omega}$ as the direction of propagation, consisting of the three components:

$$\begin{aligned} \hat{\Omega} &= (\Omega_x, \Omega_y, \Omega_z), \\ &= \left(\frac{\alpha_x}{\sqrt{\alpha_x^2 + \alpha_y^2 + 1}}, \frac{\alpha_y}{\sqrt{\alpha_x^2 + \alpha_y^2 + 1}}, \frac{1}{\sqrt{\alpha_x^2 + \alpha_y^2 + 1}} \right). \end{aligned} \tag{95}$$

Since the propagation is almost entirely in the forward direction we may approximate the vector by

$$\hat{\Omega} \approx (\alpha_x, \alpha_y, 1); \quad |\alpha_x|, |\alpha_y| \ll 1. \tag{96}$$

Since the z component of this unit vector is always approximately unity, we may ignore this component and study the tilt induced on the two-dimensional vector, $\vec{\alpha} = (\alpha_x, \alpha_y)$.

As is described in Tofsted (1989b), the unit Poynting vector associated with a propagating wavefront is just $\hat{\Omega}$. We may model the tilts induced on this wavefront as it passes through a non-uniform atmosphere by considering the gradients of the refractive index oriented perpendicular to this wave. Since the wave is propagating in primarily the z direction, these gradients are located in the (x, y) plane and affect the vector $\vec{\alpha}$. The effects of these tilts can be described by the equation

$$\frac{d\vec{\alpha}}{ds} = \frac{1}{n} \vec{\nabla}_{\perp} n, \tag{97}$$

where s is a path parameter measuring propagation distance of a point along the transverse plane in the direction of $\hat{\Omega}$, and $\vec{\nabla}_\perp$ is the gradient operator in the transverse plane. This equation represents an approximation of the results of Born and Wolf (1964, pg. 111) under the small angle assumption. Born and Wolf relate their equation to the eikonal equation, the fundamental equation of geometrical optics.

In Tofsted (1989b) the refractive index was assumed to only vary as a function of height, and this function was assumed to be attached to the surface underlying the optical path. Thus, the beam tilts induced were limited to only vertical tilt effects. These effects, however, were only evaluated for a range of elevation angles. Lehn et al. (2000, 1994, 1992) independently developed means of modifying imagery for these same effects by remapping pixels from an original scene to raytraced positions in an image plane.

The means of performing this remapping involves the reciprocity principle. According to reciprocity (van de Hulst, 1980), one can either propagate in the forward direction, from some point ($\vec{p}_0$) on the object plane in a particular initial direction ($\vec{\alpha}_0$) and attempt to shoot (cf. Press et al., 1992) a ray through the entrance pupil of the receiver system, or one may begin at the image plane and propagate a ray backwards through the volume. Eventually the backward propagating ray will intersect the object plane at a point and in a direction that would propagate through the receiver entrance pupil.

The use of deflector screens involves the replacement of the continuous form in equation (97) by a discretized version. Propagation of rays between subsequent screens is modeled as following unperturbed straight lines similar to O'Shea's (1985) equations for tracing between subsequent thin lenses. Beginning at a point $\vec{p}_m$ at the mth deflector screen, we propagate a distance Z_m to the next screen in the direction $\vec{\alpha}_m$:

$$\vec{p}_{m+1} = \vec{p}_m + \vec{\alpha}_m Z_m. \tag{98}$$

Passage through the deflector screen then perturbs the vector $\vec{\alpha}$ according to

$$\vec{\alpha}_{m+1} = \vec{\alpha}_m + \Delta\vec{\alpha}_m(\vec{p}_{m+1}), \tag{99}$$

$$\Delta\vec{\alpha}(\vec{s}) \approx \frac{1}{n_0}\vec{\nabla}_\perp\left[\int_0^\Delta n_1(\vec{s})\,dz\right], \tag{100}$$

where $1/n \approx 1/n_0$, since $n_0 \gg n_1$ in equation (61). Second, the transverse gradient operator and the path integration have been interchanged from the original form involving an integration of $\vec{\nabla}_\perp n(\vec{s})$ along the path. Third, since n_0 is constant, only n_1 appears in the gradient.

Wavefront tilt over a path increment of length Δ is effectively concentrated into an effect that is applied at a central point $\Delta/2$ into the slab. This means that the propagation distance to the first slab is $Z_1 = \Delta/2$ while the distances between

all other screens are $Z_n = \Delta$. Lastly, there is a propagation step to travel from the last slab through the receiver entrance aperture and this distance is also $\Delta/2$. Of course, when using reciprocity, these steps are actually computed in reverse order.

The deflector screen consists of a function which prescribes the values of tilts, $\Delta\vec{\alpha}$, as a function of position, $\vec{s}$, of ray arrival at the screen. In essence, O'Shea's one-dimensional thin-lenses, ray-tilt equation is replaced here by a two-dimensional ray-tilt equation dictated by the statistics of the atmospheric turbulence.

4.1.2 Diffraction Approach

The diffraction approach attempts to capture amplitude and phase distortions in addition to angle-of-arrival effects. As a consequence, the propagated field, when passed through an optical system should produce both scintillation and blurring of the propagated signal. Such improvements do not come cheaply, but under certain conditions may be unavoidable for accurate calculations. However, the computational burden may be prohibitive. Martin and Flatté (1988) required a Cray XMP supercomputer to evaluate their results for a limited size beam.

Here, we follow the discussion contained in Martin and Flatté (1988), but modify the nomenclature to avoid conflicts with the symbology elsewhere in this text. We begin with radiation of wavelength λ and wavenumber $k = 2\pi/\lambda$ propagating (again) in primarily the positive z direction. The complex amplitude of this field is given by

$$\phi = \chi \exp(-ikz). \tag{101}$$

The scalar amplitude satisfies the paraxial wave equation

$$2\,i\,k\,\frac{\partial \chi}{\partial z} + \nabla_{\perp}^2 \chi + 2\,k^2\,n_1\,\chi = 0. \tag{102}$$

To propagate through turbulence with this equation, Martin and Flatté divided the propagation into two separate effects. First, the amplitude field propagates a distance Δ through uniform media in a diffraction-limited fashion. In this intervening space $n_1 = 0$. Procedurally, this involves Fourier transforming the paraxial wave equation over the transverse axes x and y. This produces the equation

$$\frac{\partial \mathrm{X}(\vec{\sigma},\, z)}{\partial z} = -i\frac{4\pi^2\sigma^2}{2k}\mathrm{X}(\vec{\sigma},\, z), \tag{103}$$

which has the solution

$$\mathrm{X}(\vec{\sigma},\, z + \Delta_{-}) = \mathrm{X}(\vec{\sigma},\, z)\, \exp\left[-i\frac{4\pi^2\sigma^2\,\Delta}{2k}\right]. \tag{104}$$

The use of the nomenclature $z + \Delta_{-}$ anticipates the next step used to handle turbulence effects: the phase screen application.

As the term phase screen implies, the turbulence effects are concentrated into so-called "screens," or planes, of turbulence. In this case the screen is located at $z+\Delta$. At the phase screen, a portion of the wavefront passing through the screen at position $\vec{s} = (x, y)$ in the transverse plane is phase advanced by an amount $\theta(\vec{s})$. Since the effects of turbulence have been compressed into a screen of zero width, there is no need to apply diffraction effects for propagation through the screen. Thus the propagating field after passing through the phase screen is given by

$$\chi(\vec{s}, z + \Delta_+) = \chi(\vec{s}, z + \Delta_-) \exp[i\,\theta(\vec{s})]\,. \tag{105}$$

Combining effects, we have a four step propagating process:

1. Discrete Fourier transform the wave amplitude function χ across the plane perpendicular to z, resulting in the function X.
2. Perform diffraction limited propagation of X from the z plane to the $z + \Delta_-$ plane.
3. Use an inverse discrete Fourier transform to recover χ at the $z + \Delta_-$ plane.
4. Apply phase screen effects to the function χ at $z+\Delta_-$ to pass it through the screen to the $z + \Delta_+$ plane.

This process is repeated until all phase screens have been crossed and the receiver aperture plane reached.

4.2 Slab Crossing Time Analysis

Note that in the previous two subsections the quantities $\theta(\vec{s})$ and $\Delta\vec{\alpha}(\vec{s})$ were critical in evaluating the effects of the turbulence upon the arriving wave field or front. The derivation of these quantities is the key topic of the remainder of this chapter. To evaluate these quantities requires analysis of beam propagation through a turbulent layer of thickness Δ. However, there are certain assumptions being made: First, we are assuming that rays passing through the slab of thickness Δ are travelling approximately parallel to one another. This simplifies the propagation integrations, but ignores the divergence of rays originating from a particular region associated with a single pixel that could pass through the entrance pupil of the receiver. But the approximation is nearly correct and will be used as a basic assumption throughout this section.

To assess $\theta(\vec{s})$ and $\Delta\vec{\alpha}(\vec{s})$ we need to first consider the fluctuations of certain propagated quantities and their correlations at different points of entry through the slab of thickness Δ. The most basic of these quantities is sometimes called the optical depth ($\Upsilon = \int_0^\Delta n\,dz$) but we prefer to analyze the time required for a ray to cross the slab ($\tau = \int_0^\Delta (n/c)\,dz$). Here, c is the speed of light in vacuum. n/c is thus the time taken by light to move a unit distance in air of refractive index n.

The analysis of beam propagation statistics begins by considering a wavefront of radiation. This same construct will be used for both the phase analysis and for the beam tilt analysis. In the former case we may envision a propagating complex amplitude wavefront χ. In the latter case we consider the light divided into a series of rays (small pencils of light, each having a small overall divergence in solid angle and a small transverse extent as it passes through a turbulent plane of interest).

Our main object of consideration is the time required for an arbitrary wavefront or ray, at a particular transverse position $\vec{s}$, to pass through a slab of intervening atmosphere of thickness Δ. This crossing time is written as

$$\tau = \int_{z}^{z+\Delta} \frac{n(\vec{s},\, z')}{c}\, dz'. \tag{106}$$

The starting position of the beam is $(\vec{s}, z) = (x, y, z)$. The ending position is $(\vec{s}, z + \Delta)$, where we ignor transverse displacements.

For our purposes we are not directly interested in τ. Rather, we are interested in the quantity

$$\delta\tau(\vec{s}) = \int_{z}^{z+\Delta} \frac{n_1(\vec{s},\, z')}{c}\, dz', \tag{107}$$

which measures the perturbation of τ about a mean transit time. Both τ and $\delta\tau$ evaluations assume propagation along the positive z axis. Of course, $\delta\tau \ll \tau$ since $n_1 \ll n_0$. Nevertheless, the slight deviations of n_1 are critical in assessing turbulence effects.

Paralleling phase screen analyses (cf. Fleck et al., 1976), we wish to evaluate a cross correlation function between the time of transit of two parallel rays crossing the slab at points $\vec{s}_1$ and $\vec{s}_2$, written as

$$\begin{aligned} r_{\delta\tau}(\vec{s}_1,\, \vec{s}_2) &= \Big\langle \delta\tau(\vec{s}_1)\, \delta\tau(\vec{s}_2) \Big\rangle \\ &= \left\langle \int_{z}^{z+\Delta} dz_1 \int_{z}^{z+\Delta} dz_2\, \frac{n_1(\vec{s}_1,\, z_1)}{c}\, \frac{n_1(\vec{s}_2,\, z_2)}{c} \right\rangle \\ &= \int_{z}^{z+\Delta} dz_1 \int_{z}^{z+\Delta} dz_2 \left\langle \frac{n_1(\vec{s}_1,\, z_1)}{c}\, \frac{n_1(\vec{s}_2,\, z_2)}{c} \right\rangle. \end{aligned} \tag{108}$$

Here, the expectation operator being applied to the entire integral is passed through the integration operators and applied directly to the n_1 product, which is permissable because the bounds of the integration are unaffected

by the expectation operator. Under a homogeneous and isotropic turbulence assumption, we may use Γ_n:

$$\left\langle \frac{n_1(\vec{s}_1,\, z_1)}{c}\, \frac{n_1(\vec{s}_2,\, z_2)}{c} \right\rangle = \frac{1}{c^2}\, \Gamma_n \left(\sqrt{|\vec{s}_1 - \vec{s}_2|^2 + (z_1 - z_2)^2} \right). \tag{109}$$

We can then replace Γ_n with the inverse transform of Ψ_n (equation (91)). Also, the vector arguments of $r_{\delta\tau}$ can be replaced by the difference vector, $\vec{s} = (x_1 - x_2,\, y_1 - y_2)$:

$$\begin{aligned} r_{\delta\tau}(\vec{s}) = \frac{1}{c^2} \int_z^{z+\Delta} dz_1 \int_z^{z+\Delta} dz_2 \iint_{-\infty}^{\infty} \exp[i\, 2\pi\, \vec{\sigma} \cdot \vec{s}]\, d\vec{\sigma} \\ \times \int_{-\infty}^{\infty} \exp[i\, 2\pi\, \xi_z (z_1 - z_2)]\, \Psi_n \left(\sqrt{|\vec{\sigma}|^2 + \xi_z^2} \right)\, d\xi_z, \end{aligned} \tag{110}$$

where $\vec{\sigma}$ represents the two-dimensional vector components of $\vec{\xi}$ in the transverse plane, and ξ_z represents the component along the propagation axis.

This form permits a change in the order of integration such that the z integrations are accomplished first. To perform these integrations we will revert to the variable $\kappa_z = 2\pi\xi_z$ to make the mathematics somewhat simpler:

$$\int_z^{z+\Delta} dz_1 \int_z^{z+\Delta} dz_2\, \exp\left[i\kappa_z (z_1 - z_2)\right] = 2 \left[\frac{1 - \cos(\kappa_z \Delta)}{\kappa_z^2} \right], \tag{111}$$

assuming $\Delta > 0$. Fleck et al. (1976) obtain this same result through a different method: In their discussion they introduce absolute value signs around the difference $z_1 - z_2$. Possibly this is because Γ_n is a function of distance, r, which is positive definite, but this should not matter since Γ_n is spherically symmetric. Unfortunately, the introduction of the absolute value complicates the integration such that they generate an imaginary term. They must then argue away this imaginary term before they can arrive at a result equivalent to equation (111).

Fleck et al. (1976) then assume that as long as Δ is large compared to correlation lengths of the refractive index power spectrum, and as long as the spectrum is slowly varying, the ξ_z integral may be approximated as

$$\begin{aligned} &\int_{-\infty}^{\infty} \Psi_n\, (\vec{\sigma},\, \xi_z)\, \frac{2}{\kappa_z^2}\, [1 - \cos(\kappa_z \Delta)]\, d\xi_z \\ &\qquad = \int_{-\infty}^{\infty} \Psi_n \left(\vec{\sigma},\, \frac{\kappa_z}{2\pi} \right) \frac{2}{\kappa_z^2}\, [1 - \cos(\kappa_z \Delta)]\, \frac{d\kappa_z}{2\pi} \\ &\qquad \approx \frac{\Psi_n(\vec{\sigma},\, 0)}{2\pi} \int_{-\infty}^{\infty} \frac{2}{\kappa_z^2}\, [1 - \cos(\kappa_z \Delta)]\, d\kappa_z. \end{aligned} \tag{112}$$

Upon a change of variables, $u = \kappa_z \Delta$, Gradshteyn and Ryzhik's (1980) result 3.782 allows us to solve this integral directly, as

$$\int_{-\infty}^{\infty} \frac{2}{\kappa_z^2} \left[1 - \cos(\kappa_z \Delta)\right] d\kappa_z = \Delta \int_{-\infty}^{\infty} \frac{2\left[1 - \cos(u)\right]}{u^2} du = 2\pi\Delta. \qquad (113)$$

The approximation used in equation (112) assumed that $\Delta \gg L_o$. We may establish some sort of lower limit on the size of Δ by considering the correlations present in the function Γ_n. Figure 3 shows the structure of the covariance function with distance normalized relative to outer scale L_o. As shown, significant correlations extend to approximately 10 outer scale lengths. Beyond 10 outer scale lengths, Γ_n becomes negative but remains very small. Since these correlations extend in all directions about any point, it would appear the size of the modeled volume should be at least 20 L_o along each axis direction.

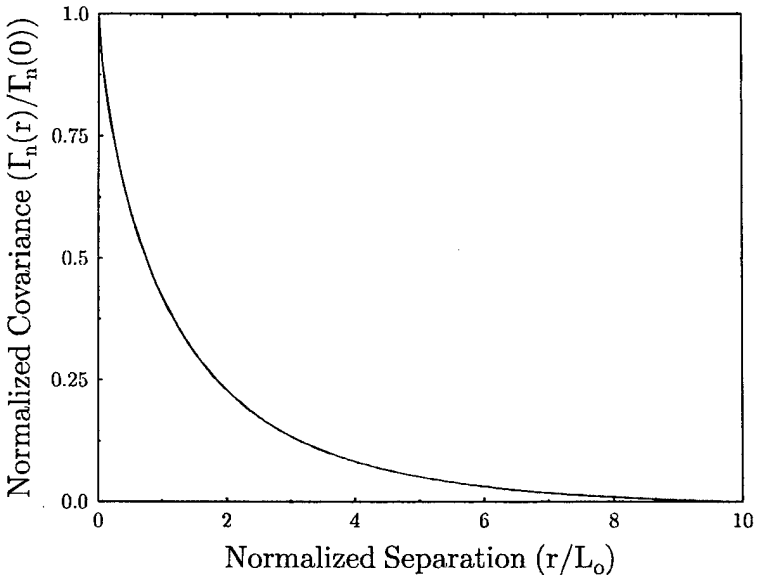

Figure 3. Covariance function normalized relative to its amplitude at zero and normalized abscissa measured relative to the outer scale length.

The size of the modeled volume is also important in that it determines the lowest frequency that can be represented. A volume that is not large enough will not be able to capture the form of the spectrum at sufficient resolution. We will return to this point when considering the resulting spectrum at the end of this analysis.

Finally, the evaluation of $r_{\delta\tau}$ thus far has reduced the problem from a five-fold integration to a two-dimensional inverse Fourier transform:

$$\begin{aligned} r_{\delta\tau}(\vec{s}) &= \frac{\Delta}{c^2} \int_{-\infty}^{\infty}\int \Psi_n(\vec{\sigma},\, 0)\, \exp[i\, 2\pi\, \vec{\sigma}\cdot\vec{s}]\, d\vec{\sigma} \\ &= \int_{-\infty}^{\infty}\int \left[\frac{\Delta\, \Psi_n(\vec{\sigma},\, 0)}{c^2}\right] \exp[i\, 2\pi\, \vec{\sigma}\cdot\vec{s}]\, d\vec{\sigma}. \end{aligned} \tag{114}$$

4.3 Crossing Time Fluctuation Spectra

Continuing to follow the arguments of Fleck et al. (1975) we recognize that $\Delta\Psi_n(\vec{\sigma},0)/c^2$ is the Fourier transform of $r_{\delta\tau}$. Let us then consider equation (108): We recognize that $r_{\delta\tau}$ is equivalent to the expectation of an autocorrelation operation, where the autocorrelation operation occurs over space and the expectation is taken over all possible atmospheres exhibiting the same turbulence spectral properties.

The random field $\delta\tau(\vec{s})$ thus defines the fluctuations in crossing times of waves propagating through the turbulent slab of thickness Δ. Let us assume that this random field has a Fourier transform $T(\vec{\sigma})$. The transform of cross correlation $r_{\delta\tau}$ must therefore be somehow connected to the average of the product $T(\vec{\sigma})\, T^*(\vec{\sigma})$ since this product represents the autocorrelation of the field $\delta\tau(\vec{s})$. However, progress in developing this relationship is only possible if we assume that $\delta\tau$ is periodic.

To begin, equation (108) can be written in terms of the difference vector $\vec{s}$: If we assume that $\delta\tau$ is periodic over a region measuring X and Y in size in the $\vec{s}$ plane, then we can define the expectation in terms of a spatial average over this fundamental periodic region as

$$r_{\delta\tau}(\vec{s}) = \left\langle \frac{1}{XY} \int_{-X/2}^{X/2}\int_{-Y/2}^{Y/2} \delta\tau(\vec{s}_2 + \vec{s})\, \delta\tau(\vec{s}_2)\, d\vec{s}_2 \right\rangle. \tag{115}$$

In this form, we see that $r_{\delta\tau}$ includes an autocorrelation function as defined for the Fourier series form, in equation (30). Let us denote by $\tilde{R}_{lm}$ the Fourier series coefficients associated with the periodic version of $r_{\delta\tau}$. If we then operate on equation (115) to generate the Fourier series coefficients associated with this equation, we obtain

$$\tilde{R}_{lm} = \left\langle \tilde{T}_{lm}\, \tilde{T}^*_{lm} \right\rangle. \tag{116}$$

But we know that taking the Fourier transform of equation (115) results in

$$r_{\delta\tau}(\vec{s}) \overset{\mathcal{F}}{\Longrightarrow} R(\vec{\sigma}) = R(\sigma_x, \sigma_y) = \frac{\Delta\Psi_n(\sigma_x, \sigma_y, 0)}{c^2}. \tag{117}$$

And, from extension of equation (48) to two dimensions, we have the following relationship between $\tilde{R}_{lm}$ and $R(\vec{\sigma})$:

$$\tilde{R}_{lm} = \frac{R\left(\frac{l}{X}, \frac{m}{Y}\right)}{XY}. \tag{118}$$

We now have $\tilde{R}_{lm}$, a Fourier series representation of $r_{\delta\tau}$. We recall from section 2.2 that the Fourier series coefficients retain the same units as the transformed function. Therefore, $\tilde{R}_{lm}$ has units of s^2. The standard method (see Fleck et al., 1975; Martin and Flatté, 1988; Davis, 1994; and Yan et al., 2000) of generating the random field $\delta\tau$ involves generating random T_{lm} values that satisfy equation (116), and then inverse transforming. Generation of random T_{lm} values involves coupling an envelope function, which defines the frequency weighting, with a white noise Gaussian random process. The resulting form for the T_{lm} coefficients is given by

$$\tilde{T}_{lm} = \overline{T}_{lm}\,\tilde{G}_{lm}. \tag{119}$$

Because $\overline{T}_{lm}$ is constant, it factors out of the expectation operator on the RHS of equation (116). Because of this property, it is standard to define $\tilde{G}_{lm}$ such that

$$\left\langle \tilde{G}_{lm}\,\tilde{G}^*_{lm} \right\rangle = 1. \tag{120}$$

Thus,

$$\overline{T}_{lm} = \sqrt{\tilde{R}_{lm}} = \sqrt{\frac{\Delta\Psi_n\left(\frac{l}{X}, \frac{m}{Y}, 0\right)}{XY\,c^2}}. \tag{121}$$

The $\tilde{G}_{lm}$ coefficients are normally represented as the sum of two zero-mean unit-variance Gaussian random variables such that $\tilde{G}_{lm}$ exhibit Hermitian properties:

$$\tilde{G}_{lm} = \frac{a_1(l,m) + i a_2(l,m)}{\sqrt{2}}. \tag{122}$$

Fleck et al. (1975) identify the following results of the Hermitian conditioning on coefficients $a_1(l,m)$ and $a_2(l,m)$:

$$\begin{aligned}
&\left\langle \hat{a}_1(l,m)\,\hat{a}_2(l,m) \right\rangle = 0; \\
&\left\langle \hat{a}_1(l,m)\,\hat{a}_1(l',m') \right\rangle = \delta_l^{l'}\,\delta_m^{m'} + \delta_l^{-l'}\,\delta_m^{-m'}; \\
&\left\langle \hat{a}_2(l,m)\,\hat{a}_2(l',m') \right\rangle = \delta_l^{l'}\,\delta_m^{m'} - \delta_l^{-l'}\,\delta_m^{-m'}.
\end{aligned} \tag{123}$$

Hence, we have random variables which are uncorrelated from point to point, and which obey the conditions

$$\hat{a}_1(l,m) = \hat{a}_1(-l,-m); \tag{124}$$

$$\hat{a}_2(l,m) = -\hat{a}_2(-l,-m). \tag{125}$$

As Davis (1994) explains, $\tilde{G}_{lm}$ "represents the Fourier transform of a grid of uncorrelated Gaussian distributed random numbers representing phases. The proper spatial structure function corresponding to turbulence statistics is imposed upon the random phases...by applying a filter...." The filter function in this case is $\overline{T}_{lm}$.

With this Hermitian conditioning we can see that $\tilde{G}^*_{lm} = \tilde{G}_{-l,-m}$. Hence we can directly show that equation (120) is valid:

$$\begin{aligned}
\langle \tilde{G}_{lm}\, \tilde{G}^*_{lm} \rangle &= \langle \hat{G}_{lm}\, \hat{G}_{-l,-m} \rangle \\
&= \left\langle \frac{[\hat{a}_1(l,m) + i\hat{a}_2(l,m)]}{\sqrt{2}} \frac{[\hat{a}_1(-l,-m) + i\hat{a}_2(-l,-m)]}{\sqrt{2}} \right\rangle \\
&= \left\langle \frac{\hat{a}_1(l,m)\hat{a}_1(-l,-m)}{2} \right\rangle + \left\langle \frac{i\hat{a}_1(l,m)\hat{a}_2(-l,-m)}{2} \right\rangle \\
&+ \left\langle \frac{i\hat{a}_2(l,m)\hat{a}_1(-l,-m)}{2} \right\rangle + \left\langle \frac{i^2\hat{a}_2(l,m)\hat{a}_2(-l,-m)}{2} \right\rangle \\
&= \frac{1 + i(0) + i(0) + i^2(-1)}{2} = 1.
\end{aligned} \tag{126}$$

These results can then be combined and used in either the phase screen or deflector screen approaches. Equation (119) can be evaluated using equations (121) and (122). The prior discussion in the section then reveals that

$$\tilde{T}_{lm} \overset{\mathcal{F}^{-1}}{\Longrightarrow} \delta\tau(\vec{s}) \tag{127}$$

over the area XY. For the phase screen problem, we recognize that $\delta\tau$ represents the extra time it takes the wavefront at position $\vec{s}$ to propagate across distance Δ compared to a mean propagation time $\overline{\tau} = \Delta\, n_0/c$. As a result, in the $z + \Delta$ plane, after the passage of time $\overline{\tau}$, at position $\vec{s}$, instead of advancing in phase by the average amount $k\Delta$, the phase only advances by $k\Delta - kc\delta\tau/n_0$. The phase delay is thus

$$\theta(\vec{s}) = k\,\frac{c}{n_0}\,\delta\tau(\vec{s}). \tag{128}$$

This phase delay appears directly in the screen propagation calculation in equation (105). To describe the equivalent effect as measured by the deflector screen approach, a more complicated analysis is required. This analysis is described in section 4.4.

4.4 Beam Deflection Analysis

We now consider the evaluation of raytracing deflector screens. From section 4.3 we know how to evaluate a random field of temporal delays $\delta\tau$. We now extend that analysis to determine how these temporal delays translate into beam tilts. Consider figure 4 where we view two transversally separated points associated with two points along a wavefront that is propagating through an atmospheric slab of thickness Δ. Due to the slight differences in the refractive index for the two paths, the transit time for each path will be slightly different. For argument's sake let us separate the two paths vertically as in the figure and assume the light travelling through the slab along the upper path takes longer than for a ray passing through along the lower path. We denote the transit time difference by $\Delta\delta\tau$. Due to the transit time difference, light on the lower path will be able to travel slightly beyond the end of the slab in the same time it takes light along the upper path to transit the slab. The mean additional propagation distance for this portion of the beam will be approximately $c\,\Delta\delta\tau/n_0$, where the contribution due to n_1 is assumed negligible ($n_1 \ll n_0$).

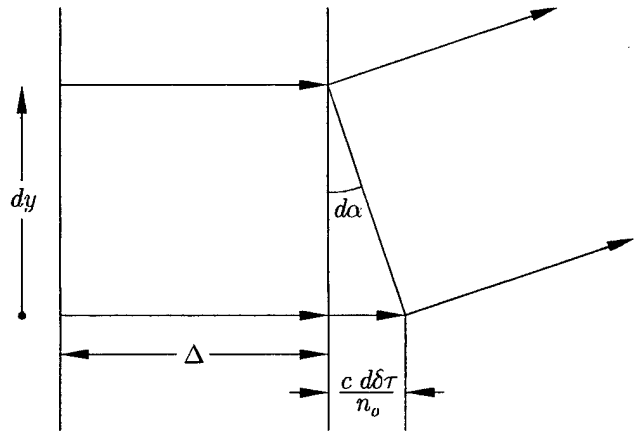

Figure 4. Ray deflection due to differential time to cross a turbulent slab.

Due to the additional propagation of the light along the lower path, the orientation of the wavefront of the beam will be slightly deflected by amount $\Delta\alpha$ upon transit through the slab. This assumes that the separation distance between the two paths (Δy) is small enough that the tilt effect is the primary modifying effect of the turbulence between these two points. The deflection

angle can then be computed as the ratio of the additional propagation length $c\,\Delta\delta\tau/n_0$ to the separation distance dy:

$$\Delta\alpha = \frac{c}{n_0}\,\frac{\Delta\delta\tau}{\Delta y}. \tag{129}$$

Let us now take the limit of this procedure as Δy approaches zero. Deflection $\Delta\alpha$ remains finite upon passage of the ray through the slab, but $\Delta y \to dy$ and $\Delta\delta\tau \to d\delta\tau$ become differentials. The differential form of this result can then be generalized to a two-dimensional deflection, such that

$$\Delta\vec{\alpha} = \frac{c}{n_0}\,\vec{\nabla}_\perp \delta\tau, \tag{130}$$

where the gradient operates in the transverse plane perpendicular to the main axis of propagation.

Representing $\delta\tau$ in terms of its Fourier series coefficients $\tilde{T}_{lm}$, we see that $\delta\tau$ can be evaluated at an arbitrary location via

$$\delta\tau(x,y) = \sum_{l=-\infty}^{\infty}\sum_{m=-\infty}^{\infty} \tilde{T}_{lm}\,\exp\left[i\,2\pi\left(\frac{lx}{X}+\frac{my}{Y}\right)\right]. \tag{131}$$

In this form, the gradient operator can be evaluated directly within the Fourier representation itself to produce

$$\begin{aligned}\Delta\vec{\alpha}(x,y) &= \frac{c}{n_0}\,\vec{\nabla}_\perp\delta\tau \\ &= \frac{c}{n_0}\sum_l\sum_m i\,2\pi\left[\frac{l}{X}\hat{\imath}+\frac{m}{Y}\hat{\jmath}\right]\tilde{T}_{lm}\,\exp\left[i\,2\pi\left(\frac{lx}{X}+\frac{my}{Y}\right)\right].\end{aligned} \tag{132}$$

Of course, computationally speaking, we can only evaluate $\Delta\vec{\alpha}$ at a finite series of points. Under these circumstances an FFT can be used, and intermediate points can be evaluated using interpolation techniques. Equation (132) provides a means for evaluating this finite grid of deflection vectors.

This result apparently concludes our analysis. However, there is a problem. The gradient operation only applies to infinitessimally narrow rays of light. But the light received at a single pixel site within the image plane must arise from a finite area within the object plane. Also, the energy from this source region must pass through a finite-sized receiver aperture. These factors indicate that finite width beams must be considered in evaluating $\Delta\vec{\alpha}$. Elements of this issue were considered previously when evaluating beam-wave angle-of-arrival calculations in Tofsted (1992). That document contained a derivation for angle-of-arrival variance of a uniform cross-section beam. In that analysis the deflection angle was determined by considering the tilt in the beam across a distance D, which was nominally assigned to the value of the beam diameter.

A similar approach can be used here, but must be modified in light of the imaging scenario at hand. There are three aspects to these modifications: First, in equation (132) all frequencies of distortions were included in the spectral summation. However, for turbulence fluctuations whose wavelengths are comparable to or narrower than the beam width, their primary effect will be to distort the beam structure rather than to tilt its direction of propagation. Even wavelengths larger than the beam width will be less effective at causing tilt because the beam width is a sizable fraction of the wavelength. Second, we must somehow define what we mean when referring to the beam width. The emissions from the object surfaces radiate as spherical waves from a multitude of independent (incoherent) regions within the footprint of a single pixel's IFOV (Instantaneous Field Of View), ϕ_p. In the absence of excessive turbulence scattering of the propagated wave, we may designate a volume that defines the space through which the energy arising from the pixel region flows through to enter the receiver aperture. It is the characteristic width of this volume that is needed to describe the influence of a particular spatial frequency on the tilt factor $\Delta\vec{\alpha}$. Lastly, we may inquire regarding the shape of the "beam" as it travels through space. Since it is not uniformly square or circular (it metamorphoses from one shape to the other over the course of propagating from the object plane to the receiver aperture), it must have different effects for every different spatial frequency at every different position along the optical axis. Moreover, even if we considered the initial radiance pattern arising from a particular source region in the object plane as constant in magnitude, because of the morphological changes, the irradiance pattern would not remain constant within its envelope as a function of path position.

Under ideal conditions we would assume the receptor area for a single pixel would be some square region on the receiver plane (assuming square pixels). Ignoring system blur and turbulence effects, we would project that the energy falling within a single pixel would arise from an area $\phi_p^2 Z^2$ on the object plane. Assuming each point on the object plane associated with this pixel emits a spherical wave of radiance I_0, and that only the portion of this wave that enters the system aperture is significant, we can model the irradiance pattern of a pixel region in the object plane as

$$I(\vec{s},\, z) = I_0 \left[\frac{\pi D_{\odot}^2(z)}{4}\right]^{-1} \int_{-\phi_p Z/2}^{\phi_p Z/2} dx' \int_{-\phi_p Z/2}^{\phi_p Z/2} dy' \,\mathrm{cyl}\left[\frac{\vec{s} - (1 - z/Z)\,\vec{s}'}{D_{\odot}(z)}\right]; \quad (133)$$

$$\mathrm{cyl}\left(\frac{r}{D}\right) = \begin{cases} 1, & |r| < D/2; \\ 0, & |r| > D/2. \end{cases} \quad (134)$$

For convenience the pixel position was assumed to lie along the optical axis.

The meaning of this function is that a scaled version of the original projected pixel shape is convolved with a scaled version of the entrance aperture shape of the receiver. We can parameterize these results if we set $P = \phi_p Z$ and

let $P_\odot = (1 - z/Z)\,P$ be the scaled width of a square at distance z just as $D_\odot = (z/Z)\,D$ is a scaled diameter of a circle at the same position. Using this method, we have an irradiance pattern which transitions smoothly between a square pattern at the source and a circular pattern at the receiver.

We can now create two dimensionless variables $A = (D_\odot - P_\odot)/(D_\odot + P_\odot)$, $B = (D_\odot + P_\odot)/\lambda_T$, where λ_T is a single wavelength of turbulent fluctuations (either X/l or Y/m in equation (132)). Due to the separability of the turbulent effects in x and y, we can evaluate tilt efficiencies for components on each axis individually. Similar to the approach used by Fried (1965) we can evaluate an overall tilt effect on the aggregate of irradiance passing through a given layer. We evaluate this quantity as follows: From equation (132) we extract the (l, m) and $(-l, -m)$ components of the summation and combine them to produce a tilt effect for a single characteristic frequency. Let us then write $\tilde{T}_{lm}$ as a magnitude M and a complex phase θ, $\tilde{T}_{lm} = M\,e^{i\theta}$. Considering only the x axis effects we have the net component of $\Delta\vec{\alpha}$ in the x direction of

$$\Delta\alpha_{x\,lm}(\vec{s}) = \frac{M\,l}{X}\,\cos\left[\frac{\pi}{2} + \theta + 2\pi\left(\frac{lx}{X} + \frac{my}{Y}\right)\right]. \tag{135}$$

We simplify this result by considering only a component along the x axis ($m = 0$). This step is necessary to simplify the mathematics, but can be seen to be possible for any value of m by a rotation of axes. We can then write

$$\Delta\alpha_{x\,lm}(\vec{s}) = -\frac{M}{\lambda_T}\,\sin\left[\theta + \frac{2\pi\,x}{\lambda_T}\right]. \tag{136}$$

A dimensional analysis of equation (132) reveals M has units of length. To determine the mean angular tilt of a beam, we need to weigh the amount of the tilt (here $\Delta\alpha_{x\,lm}$) by the amount of energy being affected at every point in the beam:

$$\overline{\Delta\alpha}(\lambda_T,\,\theta) = \frac{\int\int \Delta\alpha_{x\,lm}(\vec{s})\,I(\vec{s},\,z)\,d\vec{s}}{\int\int I(\vec{s},\,z)\,d\vec{s}}. \tag{137}$$

This evaluation determines the average deflection of the beam for a particular value of θ, but to determine the overall efficiency of the turbulence wavelength λ_T in deflecting radiation, this result needs to be averaged over all possible values of θ. Further, since $\Delta\alpha$ is a zero mean variable, it will be necessary to consider the second moment in seeking a meaningful statistic:

$$\left\langle \overline{\Delta\alpha}^2(\lambda_T) \right\rangle = \frac{1}{2\pi}\int_0^{2\pi} \overline{\Delta\alpha}^2(\lambda_T,\,\theta)\,d\theta. \tag{138}$$

The last step in this analysis is to normalize equation (138) by dividing by the value of the said measure when the irradiance profile approaches zero width. Evaluation of this case yields the limiting value $M^2/(2\,\lambda_T^2)$.

However, we are not interested in the efficiency of generating $\Delta\alpha^2$, but $\Delta\alpha$, so the final efficiency metric chosen should be proportional to the square root of the former quantity:

$$\epsilon = \sqrt{\frac{2\left\langle \overline{\Delta\alpha}^2(\lambda_T)\right\rangle}{[M^2/\lambda_T^2]}}. \tag{139}$$

Here, efficiency ϵ depends on both A and B, where A characterizes the shape of the irradiance pattern and B indicates the relative size of the pattern to the turbulence wavelength. For the case of a square pattern $A = -1$, and one can derive

$$\epsilon = \frac{|\sin(\pi B)|}{\pi B} = |\mathrm{sinc}(B)|. \tag{140}$$

For a circular pattern $A = +1$, and one can derive

$$\epsilon = 2\frac{|J_1(\pi B)|}{\pi B}. \tag{141}$$

These functions are very similar in appearance though the zeros occur at different intervals and the patterns extinguish at different rates.

In evaluating the more general cases, we note that the factor M/λ_T drops out when dividing by $1/2\, M^2/\lambda_T^2$. Second, using the rule $\sin(a+b) = \sin(a)\,\cos(b) + \cos(a)\,\sin(b)$, we may expand the term $\sin(\theta + 2\pi\, x/\lambda_T)$ and represent the evaluation in terms of two integrals to evaluate equation (137). Of these two, one will contain the term $\sin(2\pi\, x/\lambda_T)$, and because sinc is an odd function, while the irradiance pattern is even, the net integral must evaluate to zero.

The remaining term in equation (137) involves a $\sin(\theta)$ quantity which factors out of the integral. Equation (138) is thus considerably simplified and yields the result $(2\pi)^{-1}\int_0^{2\pi}\sin^2(\theta)\,d\theta = 1/2$. (Note: This $1/2$ factor cancels with the $1/2$ in the normalizing factor.) We then further normalize the integration procedure by the changes of variables $x = \lambda_T B u$ and $y = \lambda_T B v$. These substitutions result in an argument of $2\pi B u$ in the cosine variable and to normalized limits for the integration region of the irradiance signature:

$$\epsilon(A,\, B) = \left| \int_{-1/2}^{1/2} \cos(2\pi B u)\, I_n(A,\, B,\, u)\, du \right|, \tag{142}$$

where I_n is a normalized irradiance pattern involving a final simplification whereby the v variable is integrated out. The resulting integral equation can be rapidly evaluated numerically for a series of patterns with different A parameter

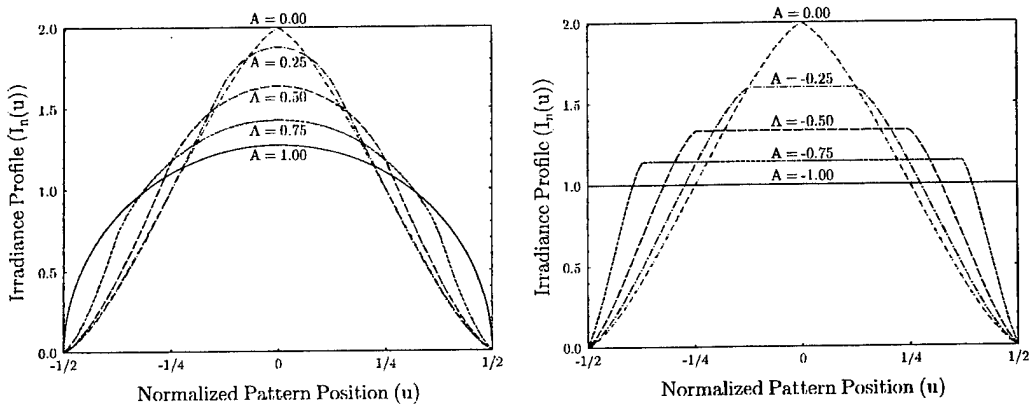

Figure 5. Normalized irradiance profiles plotted for various values of the parameter A. The area under each curve equals unity. The normalized profile position variable u ranges over the width of the pattern from -1/2 to +1/2.

values. We present a series of I_n patterns plotted for $A = -1...1$ in steps of $1/4$ in figure 5.

Use of the normalized irradiance profiles permits us to evaluate the efficiency factor using the integral relation

$$\epsilon(A,\, B) = \left| \int_{-1/2}^{1/2} \cos(2\pi B u)\, I_n(A,\, u)\, du \right| . \tag{143}$$

Resulting efficiency curves for the cases included in figure 5 are plotted in figure 6.

Since we have previously noted that the effects of beam shape can be assessed independently for each axis, we now write the final equation for $\Delta\vec{\alpha}$ by inserting efficiency factors $\epsilon(A,\, B)$ for each axis into our $\Delta\vec{\alpha}$ equation:

$$\begin{aligned} \Delta\vec{\alpha}(x,y) = \frac{c}{n_0} \sum_l \sum_m & i\,2\pi \left[\frac{l}{X}\hat{\imath} + \frac{m}{Y}\hat{\jmath} \right] \tilde{T}_{lm} \\ & \times \epsilon\left(A(z),\, lC(z)/X\right) \epsilon\left(A(z),\, mC(z)/Y\right) \\ & \times \exp\left[i\,2\pi \left(\frac{lx}{X} + \frac{my}{Y} \right) \right], \end{aligned} \tag{144}$$

where $C(z) = P_{\odot}(z) + D_{\odot}(z)$ is introduced.

Though the deflector screen model cannot handle scintillation effects, influences of wavefront degradation can be approximated by subsampling the arriving radiance over the system entrance pupil. This subsampling procedure is necessary when the turbulent coherence diameter is markedly smaller than the

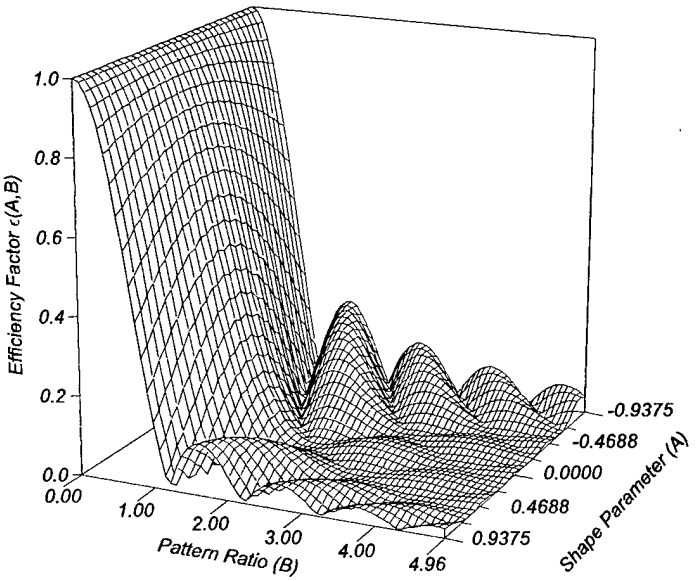

Figure 6. Efficiency response function, ϵ, plotted as a function of the shape parameter A and the pattern ratio B. The range of A values plotted indicates the behavior of the efficiency across intermediate conditions spanning between the limiting cases.

system entrance pupil diameter. In effect, different portions of the entrance pupil are seeing light arriving from a single direction that originated from different pixel regions in the object plane. Thus, it is possible to include simulated blurring effects by subsampling the entrance pupil. To determine if such subsampling is necessary, a coherence diameter (r_o) can be computed and compared with the system entrance pupil diameter (D). If the ratio $D/r_o > 1$, subsampling will be necessary. A similar comparison can be made between a coherence diameter (r_{oo}), calculated using a path weighting function oriented toward the object plane, and the width $P = Z\phi_p$. If $P/r_{oo} > 1$, it will be necessary to subsample angular trajectories within the field of regard of each pixel.

The effect of subsampling either or both of these regions would be to reduce P and/or D by factors $\sqrt{N_p}$ and/or $\sqrt{N_d}$, respectively. Call these new subsampled scales P' and D'. When subsampling the receiver aperture it would be necessary to average the sample results obtained to produce a mean result for each pixel based on the source regions mapped to by the N_d samples. From the above discussion, it would be necessary to consider the shape of the subsamples as well as their number. For subsamples in the source pixel region, it would be more advantageous to subdivide it into equal-shaped squares. For subsamples in a circular receiver aperture it might be more advantageous to model the effects in terms of hexagons which have the approximate shape of circles.

Having performed this analysis, we may be able to determine which spectral region has the most effect on tilt. For the moment let us consider the case of small pixels and a large system aperture. In this case the shape of the spectral profile

fits the case $A = 1$ over nearly the entire path. Hence, based on equation (144), the magnitude of the $\Delta\vec{\alpha}$ kernel is approximately proportional to

$$\left|\vec{\aleph}\right| \propto \sigma \sqrt{\Psi_n(\sigma)}\, \epsilon[1, \sigma C(z)]. \tag{145}$$

In this equation we have approximated the effect of either of the two orthogonal Bessel functions by a single radially symmetric ϵ function. We have also assessed the radial behavior of the gradient operator as being proportional to the magnitude of the vector. The resulting magnitude is just the modulus of the Fourier transform of $\Delta\vec{\alpha}$, here written as $\vec{\aleph}$. We show sample plots of this function in figure 7. We have plotted curves for values of L_o that are $10\,D_z$, $100\,D_z$, and $1000\,D_z$.

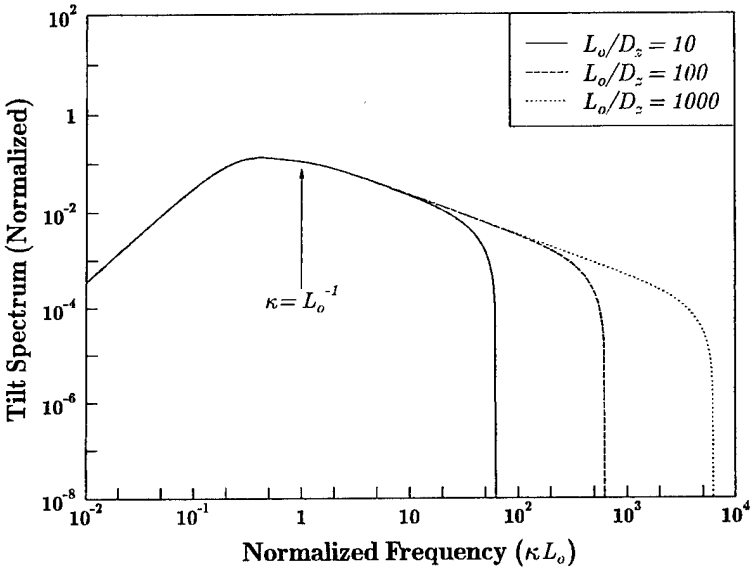

Figure 7. Proportional magnitude of the Fourier spectrum of the beam deflections normalized with respect to the outer scale length.

As can be seen, finite pixels and entrance apertures tend to negate the efficiency of higher frequency turbulence in creating beam tilt. However, the highest frequency components obviously do not generate the greatest influence on the tilt. Rather, it is spectral components in the vicinity of the outer scale that dominate tilt effects.

4.5 Method Comparison

Before concluding, it is worthwhile to mention that the temporal cross correlation, $r_{\delta\tau}$, derived in section 4.2 is equivalent to the optical path length cross correlation derived by Fleck et al. (1975) and Martin and Flatté (1988)

except for changes in nomenclature. Nevertheless, there is a slight discontinuity between these results and those of Goodman (1985).

To study this discontinuity we must begin by translating between our nomenclature and that used by these other authors. Martin and Flatté (1988) develop a phase correlation function, B_θ, which is very similar to the Γ (optical depth) correlation analysis of Fleck et al. (1976). The use of the B convention for covariances is standard throughout a significant portion of the available literature (cf. Beland, 1993). Martin and Flatté's B_θ is proportional to our $r_{\delta\tau}$ function:

$$B_\theta(\vec{s}) = k^2\, c^2\, r_{\delta\tau}(\vec{s}). \tag{146}$$

B_θ thus equals a set of scaling constants times the 2-D inverse transform of $\Phi_n(\vec{\kappa}_t,\, 0)$. Hence, taking the forward transform of B_θ produces their function

$$\Phi_\theta(\vec{\kappa}_\perp) = 2\pi\, k^2\, \Delta\, \Phi_n(\vec{\kappa}_\perp,\, 0), \tag{147}$$

where $\vec{\kappa}_\perp$ is the transverse plane component of their $\vec{\kappa}$ frequency variable. Φ_θ is thus the 2-D power spectrum for phase fluctuations.

Previously we discussed the factor $2\pi\Delta$, indicating that the range step Δ was bounded both above and below. We now note a comparison between this result and a result for a similar analysis by Goodman (1985). Goodman's power spectrum of phase (Goodman's equation (8.6-25)) is written as,

$$F_S(\kappa_\perp;\, \Delta) = \pi \overline{k}^2 \Delta \left[1 + \frac{\sin(\kappa_\perp^2\, \Delta/\overline{k})}{\kappa_\perp^2\, \Delta/\overline{k}}\right] \Phi_n(\vec{\kappa}_\perp,\, 0). \tag{148}$$

The relationship between Φ_θ and F_S should be one-to-one, but Goodman's F_S function contains a term that depends on the dimensionless variable $u = \kappa_\perp^2\, \Delta/\overline{k}$. In the limit as $u \to 0$ this term approaches 2, which agrees with Martin and Flatté. But for large u, the term fluctuates about unity. Hence, for accurate evaluation of the phase screen and deflector screen approaches we must ensure that $\Delta \ll \overline{k}/\kappa_\perp^2$ in addition to our other conditions. Goodman's analysis is also instructive in that his results indicate that the mean wavenumber of the receiver has an influence on the overall requirements of the wave propagation methods used.

5. Conclusions

In this document two key methodologies for simulating the propagation of imagery through optical turbulence have been presented in a comprehensive analysis. The mathematical basis for such analysis rests upon the various forms of the Fourier transform, including Fourier series expansions for periodic functions and FFTs for sampled functions. Based on these Fourier methods it was shown that various means of representing the turbulent refractive index power spectrum exist, and the interrelationships between these expressions were described, particularly between the form commonly used in turbulence analysis literature and the form useful in FFT calculations.

A derivation was also presented for evaluating the propagation statistics of cross correlation of fluctuations in the time of transit of wave energy through a turbulent layer of thickness Δ. Two methods were described, one supporting wave optical calculations known as the phase screen approach, and a second method based on raytracing called the deflector screen approach.

The phase screen method is more accurate because it treats the propagating energy using wave optics. However, this method may be prohibitively more expensive in computational time as the fluctuations in the field must be tracked with high precision at each integration step. By comparison, the tilt effects modeled by the deflector screen method account for the largest energy portion of the turbulence spectrum and should be sufficient to capture large scale distortions of objects due to turbulence. The limitation is that the deflector screen method cannot properly handle turbulent scintillation or image blurring effects because only the tilt of the beam is considered, not turbulent destruction of the propagating wavefront, or loss of wavefront coherence. For far-IR systems such effects are not critical. To determine the limits of applicability of the deflector screen method it is recommended that the phase screen approach be used as a benchmark. With regard to processing requirements the deflector screen method will likely provide sufficient accuracy while providing rapid processing capability in support of scenario generation for user perception testing. The phase screen method, on the other hand, will require very high-powered computer capabilities in support of realistic propagation studies. The result will likely be that the phase screen method will see limited use, but will provide valuable information, while the bulk of the processing is accomplished using the deflector screen method which is computationally much more efficient.

References

Andrews, L.C., and B.K. Shivamoggi, 1999,*Integral Transforms for Engineers*, SPIE Optical Engineering Press, Bellingham, WA.

Beland, R.R., 1993, "Propagation through Atmospheric Optical Turbulence," chapter 2 of volume 2 of *The Infrared & Electro-Optical Systems Handbook, Atmospheric Propagation of Radiation*, F.G. Smith, ed., SPIE Optical Engineering Press, Bellingham, WA, pp. 157-232.

Borgman, L.E., 1969, "Ocean wave simulation for engineering design," *ASCE, J. Waterways and Harbors Div.*, **WW4**:556-583.

Born, M., and E. Wolf, 1964, *Principles of Optics*, Pergamon Press, New York, NY.

Clifford, S.F., 1978, "The Classical Theory of Wave Propagation in a Turbulent Medium," chapter 2 of *Laser Beam Propagation in the Atmosphere*, J.W. Strohbehn, ed., Springer-Verlag, Berlin, FRG.

Davis, C.A., 1994, *Computer simulation of wave propagation through turbulent media*, Naval Postgraduate School dissertation, Monterey, CA.

Davis, C.A., and D.L. Walters, 1994, "Atmospheric inner-scale effects on normalized irradiance variance," *Appl. Opt.*, **33**:8406-8411.

Fleck, J.A., J.R. Morris, and M.J. Feit, 1975, *Time-dependent propagation of high energy laser beams through the atmosphere*, UCRL-51826, Lawrence Livermore Laboratory, Univ. of Cal., Livermore, CA 94550.

Fleck, J.A., J.R. Morris, and M.J. Feit, 1976, *Time-dependent propagation of high-energy laser-beams through atmosphere*, *Appl. Phys.*, **10**:129-160.

Fried, D.L., 1965, "Statistics of a Geometric Representation of Wavefront Distortion," *J. Opt. Soc. Am.*, **55**:1427-1435.

Fried, D.L., 1982, "Anisoplanatism in adaptive optics," *J. Opt. Soc. Am.*, **72**:52-61.

Gaskill, J.D., 1978, *Linear Systems, Fourier Transforms, and Optics*, J. Wiley & Sons, New York, NY.

Goodman, J.W., 1985, *Statistical Optics*, J. Wiley & Sons, Inc., New York, NY.

Gradshteyn, I.S., and I.M. Ryzhik, 1980, *Table of Integrals, Series, and Products*, translated and edited by Alan Jeffrey, Academic Press, Inc., Orlando, FL.

Harris, F.J., 1978, "On the Use of Windows for Harmonic Analysis with the Discrete Fourier Transform," *Proceedings of the IEEE*, **66**:51-83.

Hinze, J.O., 1987, *Turbulence*, McGraw-Hill Inc., New York, NY.

Kolmogorov, A.N., 1962, "A refinement of previous hypotheses concerning the local structure of turbulence in a viscous incompressible fluid at high Reynolds number," *J. Fluid Mech.*, **13**:82-85.

Kolmogorov, A.N., and S.V. Fomin, 1970, *Introductory Real Analysis*, translated by R.A. Silverman, Dover Publications, Inc., New York, NY.

Kreyszig, E., 1972, *Advanced Engineering Mathematics*, J. Wiley and Sons, Inc., New York, NY.

Lehn, W.H., 2000, "Skerrylike mirages and the discovery of Greenland," *Appl. Opt.*, **39**:3612-3619.

Lehn, W.H., W.K. Silvester, and D.M. Fraser, 1994, "Mirages with atmospheric gravity waves," *Appl. Opt.*, **33**:4639-4643.

Lehn, W.H., and W. Friesen, 1992, "Simulation of mirages," *Appl. Opt.*, **31**:1267-1273.

Ludeman, L.C., 1986, *Fundamentals of Digital Signal Processing*, J. Wiley & Sons, New York, NY.

Martin, J.M., and S.M. Flatté, 1988, "Intensity image and statistics from numerical simulation of wave propagation in 3-D random media," *Appl. Opt.*, **27**:2111-2126.

O'Shea, D.C., 1985, *Elements of Modern Optical Design*, J. Wiley & Sons, New York, NY.

Panofsky, H.A., and J.A. Dutton, 1984, *Atmospheric Turbulence: models and methods for engineering applications*, J. Wiley & Sons, New York, NY.

Papoulis, A., 1984, *Probability, Random Variables, and Stochastic Processes*, McGraw-Hill Book Co., New York, NY.

Press, W. H., S. A. Teukolsky, W. T. Vetterling, and B. P. Flannery, 1992, *Numerical Recipes in C*, Cambridge Univ. Press, Cambridge, England.

Shinozuka, M., and C.-M Jan, 1972, "Digital simulation of random processes and its applications," *J. Sound and Vibration*, **25**:111-128.

Sozou, P.D., and G. Loizou, 1994, "Moving through a mirage," *Appl. Opt.*, **33**:4644-4651.

Stark, H., and J.W. Woods, 1986, *Probability, Random Processes, and Estimation Theory for Engineers*, Prentice-Hall, Englewood Cliffs, NJ.

Tatarski, V.I., 1961, *Wave Propagation in a Turbulent Medium*, R.A. Silverman, translator, McGraw-Hill Book Company, Inc., New York.

Tofsted, D.H., 1987, *EOSAEL 87, Volume 25, Optical Path Bending Code Module REFRAC*, ASL-TR-0221-25, U.S. Army Atmospheric Sciences Laboratory, White Sands Missile Range, NM.

Tofsted, D.H., 1989a, *Evaluation of the REFRAC Refractive Raytracing Algorithm*, ASL-TR-0242, U.S. Army Atmospheric Sciences Laboratory, White Sands Missile Range, NM, March 1989.

Tofsted, D.H., 1989b, *Refractive Raytrace Modeling Over Variable Terrain*, ASL-TR-0250, U.S. Army Atmospheric Sciences Laboratory, White Sands Missile Range, NM, July 1989.

Tofsted, D.H., 1992, "Outer-scale effects on beam-wander and angle-of-arrival variances," *Appl. Opt.*, **31**:5865-5870.

Tofsted, D.H., 2000, *Turbulence Simulation: Outer Scale Effects on the Refractive Index Spectrum*, ARL-TR-548, U.S. Army Research Laboratory, White Sands Missile Range, NM.

van de Hulst, H.C., 1980, *Multiple Light Scattering: Tables, Formulas, and Applications*, Academic Press, New York, NY.

von Kármán, T., 1948, "Progress in the statistical theory of turbulence," *Proc. Natl. Acad. Sci. U.S.*, **34**:530-539.

Yan, H.-X., S.-S. Li, De-L. Zhang, and S. Chan, 2000, "Numerical simulation of an adaptive optics system with laser propagation in the atmosphere," *Appl. Opt.*, **39**:3023-3031.

Acronyms

EOSAEL	Electro-Optical Systems Atmospheric Effects Library
FLIR	Forward-Looking Infrared
FFT	Fast Fourier Transform
IFOV	instantaneous field of view
IR	infrared
LSI	linear shift invariant
MFT	modulation transfer function
RHS	right hand side

Distribution

	Copies
NASA MARSHALL SPACE FLT CTR ATMOSPHERIC SCIENCES DIV SDO1 ATTN DR FICHTL HUNTSVILLE AL 35802	1
NASA SPACE FLT CTR ATMOSPHERIC SCIENCES DIV CODE ED 41 1 HUNTSVILLE AL 35812	1
US ARMY MISSILE CMND AMSMI RD AS SS ATTN MR H F ANDERSON REDSTONE ARSENAL AL 35898-5253	1
US ARMY MISSILE CMND AMSMI RD AS SS ATTN MR B WILLIAMS REDSTONE ARSENAL AL 35898-5253	1
US ARMY MISSILE CMND AMSMI RD DE SE ATTN MR GORDON LILL JR REDSTONE ARSENAL AL 35898-5245	1
US ARMY MISSILE CMND REDSTONE SCI INFO CTR AMSMI RD CS R DOC REDSTONE ARSENAL AL 35898-5241	1
US ARMY MISSILE CMND AMSMI REDSTONE ARSENAL AL 35898-5253	1

PACIFIC MISSILE TEST CTR
GEOPHYSICS DIV
ATTN CODE 3250
POINT MUGU CA 93042-5000 1

ATMOSPHERIC PROPAGATION BRANCH
SPAWARSYSCEN SAN DIEGO D858
49170 PROPAGATION PATH
SAN DIEGO CA 92152-7385 1

METEOROLOGIST IN CHARGE
KWAJALEIN MISSILE RANGE
PO BOX 67
APO SAN FRANCISCO CA 96555 1

NCAR LIBRARY SERIALS
NATL CTR FOR ATMOS RSCH
PO BOX 3000
BOULDER CO 80307-3000 1

HEADQUARTERS DEPT OF ARMY
DAMI POI
ATTN LEE PAGE
WASHINGTON DC 20310-1067 1

US ARMY INFANTRY
ATSH CD CS OR
ATTN DR E DUTOIT
FT BENNING GA 30905-5090 1

HQ AFWA/DNX
106 PEACEKEEPER DR STE 2N3
OFFUTT AFB NE 68113-4039 1

PHILLIPS LABORATORY
PL LYP
ATTN MR CHISHOLM
HANSCOM AFB MA 01731-5000 1

PHILLIPS LABORATORY
PL LYP 3
HANSCOM AFB MA 01731-5000 1

AFRL/VSBL
29 RANDOLPH RD
HANSCOM AFB MA 01731 1

ARL CHEMICAL BIOLOGY 1
NUC EFFECTS DIV
AMSRL SL CO
APG MD 21010-5423

US ARMY MATERIEL SYST 1
ANALYSIS ACTIVITY
AMSXY
APG MD 21005-5071

US ARMY RESEARCH LABORATORY 1
AMSRL D
2800 POWDER MILL ROAD
ADELPHI MD 20783-1145

US ARMY RESEARCH LABORATORY 1
AMSRL OP CI SD TL
2800 POWDER MILL ROAD
ADELPHI MD 20783-1145

US ARMY RESEARCH LABORATORY 1
AMSRL CI LL
ADELPHI MD 20783-1197

US ARMY RESEARCH LABORATORY 1
AMSRL SS SH
ATTN DR SZTANKAY
2800 POWDER MILL ROAD
ADELPHI MD 20783-1145

US ARMY RESEARCH LABORATORY 1
AMSRL CI
ATTN J GANTT
2800 POWDER MILL ROAD
ADELPHI MD 20783-1197

US ARMY RESEARCH LABORATORY 1
AMSRL
2800 POWDER MILL ROAD
ADELPHI MD 20783-1145

NATIONAL SECURITY AGCY W21 1
ATTN DR LONGBOTHUM
9800 SAVAGE ROAD
FT GEORGE G MEADE MD 20755-6000

US ARMY RSRC OFC
ATTN AMXRO GS DR BACH
PO BOX 12211
RTP NC 27009 1

DR JERRY DAVIS
NCSU
PO BOX 8208
RALEIGH NC 27650-8208 1

US ARMY CECRL
CECRL GP
ATTN DR DETSCH
HANOVER NH 03755-1290 1

US ARMY ARDEC
SMCAR IMI I BLDG 59
DOVER NJ 07806-5000 1

ARMY DUGWAY PROVING GRD
STEDP MT DA L 3
DUGWAY UT 84022-5000 1

ARMY DUGWAY PROVING GRD
STEDP MT M
ATTN MR BOWERS
DUGWAY UT 84022-5000 1

DEPT OF THE AIR FORCE
OL A 2D WEATHER SQUAD MAC
HOLLOMAN AFB NM 88330-5000 1

PL WE
KIRTLAND AFB NM 87118-6008 1

USAF ROME LAB TECH
CORRIDOR W STE 262 RL SUL
26 ELECTR PKWY BLD 106
GRIFFISS AFB NY 13441-4514 1

AFMC DOW
WRIGHT PATTERSON AFB OH 45433-5000 1

US ARMY FIELD ARTILLERY SCHOOL
ATSF TSM TA
FT SILL OK 73503-5600 1

US ARMY FOREIGN SCI TECH CTR
CM
220 7TH STREET NE
CHARLOTTESVILLE VA 22902-5396 1

NAVAL SURFACE WEAPONS CTR
CODE G63
DAHLGREN VA 22448-5000 1

US ARMY OEC
CSTE EFS
PARK CENTER IV
4501 FORD AVE
ALEXANDRIA VA 22302-1458 1

US ARMY CORPS OF ENGRS
ENGR TOPOGRAPHICS LAB
ETL GS LB
FT BELVOIR VA 22060 1

US ARMY TOPO ENGR CTR
CETEC ZC 1
FT BELVOIR VA 22060-5546 1

SCI AND TECHNOLOGY
101 RESEARCH DRIVE
HAMPTON VA 23666-1340 1

US ARMY NUCLEAR CML AGCY
MONA ZB BLDG 2073
SPRINGFIELD VA 22150-3198 1

USATRADOC
ATCD FA
FT MONROE VA 23651-5170 1

ATRC WSS R
WSMR NM 88002-5502 1

US ARMY RESEARCH LABORATORY AMSRL CI E COMP & INFO SCI DIR WSMR NM 88002-5501	1
DTIC 8725 JOHN J KINGMAN RD STE 0944 FT BELVOIR VA 22060-6218	1
US ARMY MISSILE CMND AMSMI REDSTONE ARSENAL AL 35898-5243	1
US ARMY DUGWAY PROVING GRD STEDP3 DUGWAY UT 84022-5000	1
USTRADOC ATCD FA FT MONROE VA 23651-5170	1
WSMR TECH LIBRARY BR STEWS IM IT WSMR NM 88002	1
US ARMY RESEARCH LAB AMSRL D DR D SMITH 2800 POWDER MILL RD ADELPHI MD 20783-1197	1
US ARMY CECOM INFORMATION & INTELLIGENCE WARFARE DIRECTORATE ATTN AMSEL RD IW IP FORT MONMOUTH NJ 07703-5211	1
US ARMY RESEARCH LAB ATTN AMSRL CI EW MR TOFSTED WSMR NM 88002-5513	15
Record copy	1
TOTAL	70